An Energy Efficient Thermally Regulated Optical Cell for Lab-on-Chip Devices: Applied to Nitrate and Nitrite Detection.

by

Benjamin Joseph Murphy

Submitted in partial fulfilment of the requirements
for the degree Master of Applied Science

at

Dalhousie University
Halifax, Nova Scotia
August 2023

Dalhousie University is located in Mi'kma'ki,
the ancestral and unceded territory of the Mi'kmaq.
We are all Treaty people.

Contents

LIST OF TABLES

LIST OF FIGURES

ABSTRACT

Reagent-based colourimetric analyzers that are intended to operate for significant durations in the field typically aim to conserve energy use per measurement. In many cases, the fluid under analysis must be elevated to a temperature above that of the environment to improve reaction kinetics. In these cases, it is important to minimize the amount of energy lost to the environment in the form of heat while thermally controlling the optical cell. Here, a novel method of conserving heat energy on microfluidic systems is presented. The design minimizes heat transfer to the environment by surrounding the heated optical cell on four sides with integral air-pockets, thereby creating an insulated and suspended bridge structure. This unique microfluidic design was simulated in COMSOL and then verified in a polymethyl methacrylate (PMMA) device constructed using rapid prototyping approaches. To evaluate the effectiveness of the insulated bridge approach, the insulated design is compared to a monolithic non-insulated design without air-pockets. One 25 mm absorbance cell was suspended within an insulated bridge, and one 25 mm absorbance cell was created in a slab of monolithic PMMA. To hold the insulated cell at 35 °C, 45 °C, and 55 °C, power required was reduced by 49.3% on average in simulation and 40.2% on average in experiment when compared to the standard cell. Both insulated and non-insulated cell designs were then applied to a commonly used colourimetric assay to measure nitrate. Nitrate was reduced to nitrite using the vanadium (III) chloride method, then converted to a coloured azo dye with the well-established Griess method. The colourimetric reaction kinetics were studied at 22 °C and 41 °C, resulting in 95% colour development at 225 minutes and 20 minutes, respectively. The colourimetric method was applied to insulated and non-insulated designs at 35 °C for nitrate concentrations from 0.25 µM to 50 µM. A reduction in heating energy from 195 J to 119 J was demonstrated while preserving the expected linearity and limits of detection of 20 nM. By suspending the optical cell or inlaid microchannel within a chip, the approach avoids heating the thermal mass of the rest of the device and any interconnects. This design will have broad applicability to numerous chemical protocols that rely on optical absorbance measurements performed *in situ* for marine environments.

LIST OF ABBREVIATIONS AND SYMBOLS USED

PMMA	Polymethyl Methacrylate
MEOPAR	Marine Environmental Observation, Prediction and Response Network
NSERC	Natural Sciences and Engineering Research Council
CRD	Collaborative Research and Development
UV	Ultraviolet
FIA	Flow Injection Analysis
EOF	Electro-Osmotic Flow
NED	N-(1-aphthyl)ethylenediamine Dihydrochloride
FEP	Fluorinated Ethylene Propylene
EMF	Electromagnetic Field
LED	Light Emitting Diode
PCB	Printed Circuit Board
RMSE	Root Mean Square Error
LOD	Limit-of-Detection
PID	Proportional Integral Derivative
SMU	Source Measurement Unit

CHAPTER 1 INTRODUCTION

1.1 Background: Relevance of Nutrient Monitoring

Concentrations of nitrate in the ocean naturally vary from 0.06 to 31 mg L^{-1} (1 to 500 μM) [1]. Anthropogenic sources of nitrate, such as agriculture fertilizer runoff into waterways, can lead to eutrophication, shifting ecosystems, and undesirable blooms [2], [3]. Further, the World Health Organization reports that concentrations of nitrate in excess of 50 mg L^{-1} (806 μM) are dangerous for human consumption [4]. Therefore, routine monitoring of nitrate concentrations in waterways is important for providing early warning of elevated nitrate levels. Traditionally, such nitrate measurements are taken by manually gathering samples and testing them in laboratories that support benchtop auto-analyzers; for example, the AA500 by SEAL Analytical Inc. Preserving and transporting the samples to the laboratory hinders widespread and routine monitoring of nitrate levels, as it is labor- and resource-intensive and time consuming. In the case of oceanic monitoring this can require entire ships with full crews for weeks at a time which can be very costly.

For this reason, several in situ sensors have been developed to improve the spatial and temporal resolution of nitrate measurements [5]–[10]. The fundamental detection and transduction approaches vary widely from electrochemical, bio-molecular, optical, chemical reactions, mass spectrometry, gas/liquid chromatography. Reagent-based systems continue to be used as they offer long-shelf life, lower limits of detection, and high selectivity to the target species. These wet-chemical sensors have been used to measure nanomolar levels of ammonium, nitrate, nitrite, phosphate, iron, silicate, manganese, and sulfide as reviewed recently [11], [12]. As one of the limiting nutrients, nitrate monitoring is important to understanding the health and dynamics of aquatic ecosystems.

1.2 Thesis Scope

This thesis details work toward creating a temperature regulated *in situ* nitrate sensor. Methods for detecting nitrate and microfluidic heating are outlined with a focus on *in situ*

technology. The design of a microfluidic chip with integrated heater that uses a modified version of the Griess reaction to allow nitrate to be detected through optical spectroscopy is outlined. A novel suspended optical cell design was implemented allowing the power requirement of the on-chip heater to be reduced. The design was first analytically evaluated using circuit equivalence, then simulated to account for complex geometry of the device, and finally built and tested to demonstrate the design's effectiveness.

1.3 Research Output

The worked performed in this thesis is also described in the following peer-reviewed articles and conference proceedings.

1.3.1 Journal Articles

Luy, E. A., Morgan S. C., Creelman, J. J., **Murphy, B. J.,** and Sieben, V. J. Inlaid microfluidic optics: absorbance cells in clear devices applied to nitrite and phosphate detection. *Journal of Micromechanics and Microengineering*, 30(9):15, 2020

My contribution to this research was in fabricating and testing the sensor, as well as designing the layout of its electronics. This is the same *in situ* nutrient sensor discussed in section 2 of my thesis.

Murphy, B. J., Luy, E. A., Panzica, K., Johnson, G., and Sieben, V. J. An Energy Efficient Thermally Regulated Optical Spectroscopy Cell for Lab-on-Chip Devices: Applied to Nitrate Detection. *Micromachines*, vol. 12, p. 861, Jul. 2021

1.3.2 Conference Papers

Murphy, B. J., Morgan, S. C., Luy, E. A., Creelman, J. J., and Sieben, V. J. (2019). Lab-on-a-chip Sensor of In Situ Nutrient Monitoring. OCEANS 2019, (pp. 1 – 7). Seattle, USA: The IEEE Oceanic Engineering Society.

1.4 Monitoring Nitrate In situ

Nitrate (NO_3) and nitrite (NO_2) are currently sensed in a variety of ways. While the gold standard remains benchtop colourimetry there are several commercial sensors that operate *in situ*. While these existing *in situ* sensors tend to use less accepted methods like UV spectroscopy and ion-selective electrodes that are more easily made portable, several groups are working to adapt colourimetric sensors for *in situ* measurements.

1.4.1 Optical

Nitrate inherently absorbs strongly in the UV (ultraviolet) spectrum at a wavelength of 220 nm, and therefore, optical absorbance can be used to measure nitrate concentrations directly. Commercial sensors, such as the Seabird SUNA or the YSI EXO NitraLED are readily available and utilize this method. These sensors are appealing in their simplicity. They are able to perform absorbance based measurements similar to the benchtop colourimetry methods discussed earlier without the requirement of additional reagents or complicated fluid management. However, this method brings its own set of challenges. UV measurements are influenced by matrix effects such as water colour and other absorbing species in the UV spectrum, as well as water turbidity [13]. In such systems, the sensor must delineate the attenuation and absorbance coefficients, which can be non-trivial with uncharacterized and potentially widely varying environments [14].

1.4.2 Electrochemical

Ion-selective electrodes can be used to detect nitrate ions in fluids. They operate by placing a sample solution on one side of a membrane and a reference solution on the other. The difference in ion concentration on either side of the membrane generates a voltage that can be read by a sensor. Using the Nernst equation, the measured voltage can be used to determine concentrations of nitrate ions. This method can have very fast response times as low as 2 s [15] and can detect concentration ranges as wide as 4.96 - 6.2 $\times 10^5$ μg/L (0.08 - 1 $\times 10^4$ μM). However, electrochemical nitrate measurements tend to drift significantly over time and have short lifespans. Recent efforts by Hassan et al. have seen the drift reduced to 16.6 μV/s with a sensitivity of −55.1 mV/decade, but this sensor has a limited lifespan of 8 weeks, making it impractical for long-term in situ monitoring

[16]. Such drift of the measured voltages would increase the nitrate reading to ten times its original value after 55 min of continuous operation. Commercial nitrate ISE systems, such as YSI's EXO Nitrate, have a sensitivity of 52 to 62 mV/decade and require frequent and daily calibration.

1.4.3 Colourimetric methods

The Griess assay is a process by which an aqueous sample is mixed with Griess reagent to determine the concentration of nitrite in the sample [17]. The Griess reagent, when exposed to nitrite, forms an azo dye in a concentration proportional to the amount of nitrite in the sample. Through this Griess reaction nitrite concentrations can be detected optically by directing a light through the sample and measuring how much light is blocked by the dye. The process to make Griess reagent and to perform a Griess assay are described in detail in materials and methods Section 5.1. The Beer-Lambert law dictates that the optical absorbance of the dye is linearly related to its concentration. Because of its accuracy and consistency, the Griess reaction has become the gold standard for nitrite detection and is commonly used in high end benchtop analysers [18]. To adapt this process for nitrate an additional step is required to first reduce the nitrate in the sample to nitrite before determining its concentration with the Griess assay.

This method has several complications that make it difficult to perform *in situ*. Requiring environmental samples to be mixed with Griess reagent means that the sensor must be capable of more advanced fluid handling. This also means that the sensor must carry reagent when deployed thus hampering miniaturization. To keep the sensor compact and easily deployed on space-tight sensor platforms these sensors are usually microfluidic in nature, performing measurements on fluid volumes in the µL scale.

1.5 Flow Types in Colourimetric Analysers

1.5.1 Stop Flow

In a stop flow system fluid is pumped into a reaction chamber, allowed to react for a set amount of time, then absorption spectroscopy is performed on the sample. This is the simplest flow type as stationary fluids are easy to handle and allow for samples to be developed for a user-specified amount of time. This makes it highly configurable and

permits time to react samples completely. Allowing samples to react completely reduces the frequency at which samples can be acquired but allows for lower limits of detection.

1.5.2 Continuous Flow

Continuous flow analysers determine nitrate by performing absorbance spectroscopy on moving fluids. There are two main types of continuous flow sensors: flow injection analysis (FIA) and segmented flow analysis (SFA). FIA systems operate by injecting samples periodically into a continuous flow of reagent then measuring absorbance downstream while SFA systems separate mixed sample and reagent with air bubbles. Because of these air bubbles, SFA systems are more complicated to implement than FIA and tend to be slower but they are less prone to cross talk between samples, especially for samples that need longer reaction times. Both types of continuous flow systems permit higher sample rates than stopped flow systems, with FIA systems allowing for tens of samples per hour to be measured [19], [20] whereas stopped flow schemes permit a few samples per hour [8], [21]. Continuous flow systems require more reagent because they are constantly pumping so minimizing reagent consumption is particularly important. Lab-on-chip technology and small microchannels have been utilized to perform flow injection analysis *in-situ*. Early work by Petsul et al. in 1999 demonstrated an FIA system driven by electro-osmotic flow (EOF) for nitrate using microfluidic technology on the benchtop, using only 2 μL per measurement [22]. Both stopped flow and continuous flow architectures benefit from thermal regulation of the fluid stream to control the reaction kinetics for more precise colour developments and measurements.

CHAPTER 2 IN SITU NITRITE SENSOR

This chapter outlines the design, construction, and deployment of an *in situ* nutrient sensor done in collaboration with my fellow students Joshua Creelman, Edward Luy, and Sean Morgan. This section will focus primarily on my own work while crediting my colleagues when I discuss things we worked on together or a contribution that is not my work, but important for understanding the function of the sensor. This sensor was used to detect nitrite and phosphate with my own contributions focusing on nitrite. Nitrite detection was used here as a proof of concept and first step towards developing a nitrate sensor; the necessary adjustments required to sense nitrate are discussed at the end of this chapter. It will become apparent that the addition of the novel heater design to this nitrite sensor will form the basis of a future in situ nitrate sensor.

2.1 Sensor Design

2.1.1 Microfluidic Chip Design

The microfluidic chip used in the nitrite sensor stack, shown in Figure 1, was created by Sean Morgan using a similar procedure as the chip described in chapter 4.1. The nitrite stack chip was comprised of three circular layers of PMMA. Each layer was 76 mm in diameter and 6 mm thick. The chip had two inputs, one for intaking Griess reagent and the other for intaking standards or environmental samples. These inputs led to a serpentine mixing channel followed by two inlaid absorbance cells. The two absorbance cells were of different lengths, 10 mm and 30 mm specifically. The shorter channel requires the light to pass through less liquid before reaching the detector, meaning that it will be able to detect higher concentrations of nitrite before light is blocked entirely. Conversely, the longer channel requires light to pass through more fluid allowing more light to be absorbed and lower concentrations of nitrite to be detectable by the sensor. During prototyping when misalignments in the chip's very precise optics were common this dual absorbance cell design also provided a useful layer of redundancy. This allowed

the chips to be useful for testing even if one absorbance cell failed, albeit for a smaller concentration range.

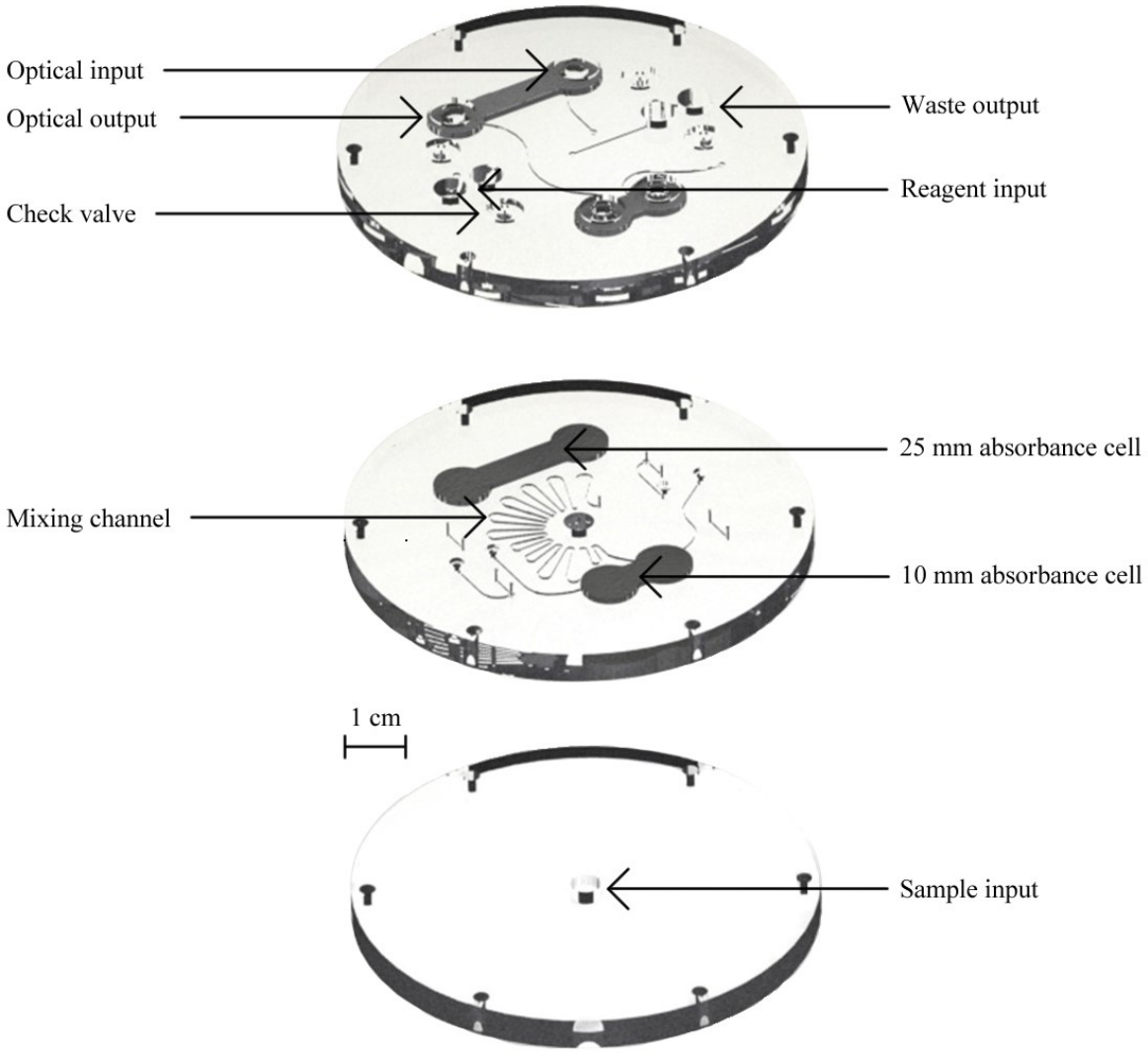

Figure 1: Exploded view of the nitrite detection chip showing the internal fluidic path. Important aspects of the design are labelled on each layer of the chip. Many of these components, like the inlaid absorbance cell, are on multiple layers but are only labelled once for clarity. The top layer, which faces into the sensor stack, contains the reagent input and waste output as well as the optical input and output. The middle layer contains the majority of the fluid channels with the mixing channel and absorbance cells. The bottom layer is the simplest with only the sample input as well as the alignment holes that are present on each layer.

2.1.2 Pumping Apparatus

Fluids were moved through the microfluidic chip using two 250 mL syringes driven by a stepper motor. Custom magnetic check valves were used to prevent backflow and ensure that the fluids would move in one direction through the chip as the syringes were filled and emptied [23]. The intake of reagent and sample were each performed using their own syringe pump. The syringes were driven using a single stepper motor and three custom milled PMMA plates as shown in Figure 2. The top and bottom plates were held stationary to create an upper and lower bound for the syringe's positions while the motor moved the middle plate up and down between them. The tops of the syringe pump's plungers were affixed to the middle plate to allow the motor to actuate both syringe pumps at the same rate. Hall effect sensors were embedded in the top and bottom plates and a magnet was embedded into the middle plate. This allowed the sensor to detect when the middle plate was approaching its upper or lower bound and stop it before it collided with another plate risking damage to the plates or motor.

2.1.3 Control Method

The sensor was controlled using a Raspberry Pi Zero W (Raspberry Pi Foundation, Cambridge, England, UK) which communicated with the rest of the stack through a custom PCB (printed circuit board). The PCB handled voltage regulation, analog-to-digital conversion (24-bit ADC), digital-to-analog conversion (16-bit DAC), timekeeping, and motor control. The motor controller required a 12 V input while the others required a 5 V input. By using a voltage regulator, a single 12 V source was used to power all of these components, greatly simplifying how the sensor was powered. The analogue to digital converter was used to allow the Raspberry Pi to read the outputs of analogue components like the photodiodes and hall effect sensors. The digital-to-analog converter was used to allow the Raspberry Pi to control a constant current source that in turn drove the LED intensity. The constant current source was necessary to ensure that no additional noise was introduced in the light intensity of the LED from an inconsistent input. An external clock chip powered by a dedicated coin cell battery was included on the PCB to allow the sensor to keep accurate time even when the sensor is shut off. Finally, a motor

controller chip was used to allow the Raspberry Pi to control the speed and direction of the stepper motor's movement through digital outputs.

The functions of the sensor were programmed into the Raspberry Pi through a custom scripting language developed by Joshua Creelman in C. Through this scripting language the Raspberry Pi could read a text file of commands and execute the commands sequentially.

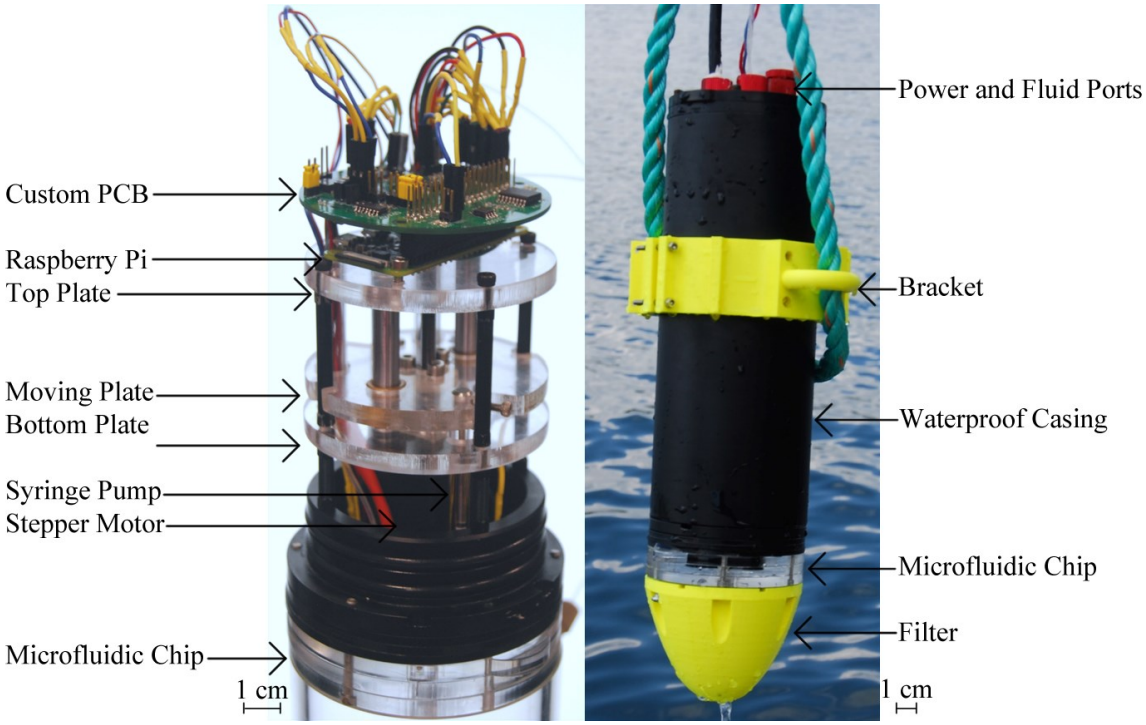

Figure 2: (Left) Sensor stack without external casing showing the internals of the experimental sensor. (Right) Watertight sensor stack as it was deployed. Important components are labelled in each picture. Scale bars are shown at the bottom of each image. The sensors are pictured at slight angles so while scale is shown at the bottom of each image it is not entirely consistent within images.

2.2 Benchtop Calibration

Prior to *in situ* testing, the sensor needed to be calibrated under controlled conditions to know the relationship between photodiode voltage output and nitrite concentration. Because minute differences in optical alignment can have significant effects on photodiode output the device needed to be recalibrated any time it was assembled. These calibrations also act as tests of the device's functionality. A correctly functioning device will show a linear relationship between concentration and absorbance in accordance with the Beer-Lambert law.

2.2.1 Data Collection Procedure

Before performing the benchtop calibration the syringe pumps were primed by manually pumping milli-Q water through both pumps to ensure that no air or dye from previous tests were present in the channels. Next, the reagent bag was attached to the reagent input and the waste bag was attached to the waste output. The sample input was attached to a 10-port Vici Cheminert selector valve (Valco Instrument Co. Inc. Houston TX USA) which could be set up to autonomously switch between the 8 sample concentrations, 0.1, 0.25 µM, 0.5 µM, 1 µM, 2 µM, 5µM, 10 µM, 20 µM and milli-Q water. The sensor was scripted to take measurements using each concentration beginning with the lowest concentration and working up to avoid inter sample cross-talk which can be a problem when taking low concentration measurements directly after high concentration measurements. Between each sample measurement a blank measurement was taken using milli-Q water. Measurements were taken by having the sensor pump fluid for 1 min then waiting 5 mins for the dye to finish developing while continuously polling the photodiodes. The last 60 datapoints were averaged to mitigate noise in the measurement. Following this the LEDs were turned off and the photodiodes were polled for 30 s and averaged to determine the dark reference which was subtracted from the sample measurement to remove error from extraneous light. The average photodiode output was then compared with the average output from the previous blank measurement to get an absorbance value for that concentration. Data generated from this process is shown in Figure 3. With an R^2 value of 0.9996, this data demonstrates a high level of linearity between concentration and absorbance in accordance with the Beer-Lambert law. This

indicated that the sensor stack was functioning correctly in a laboratory setting and was ready to be deployed *in-situ*.

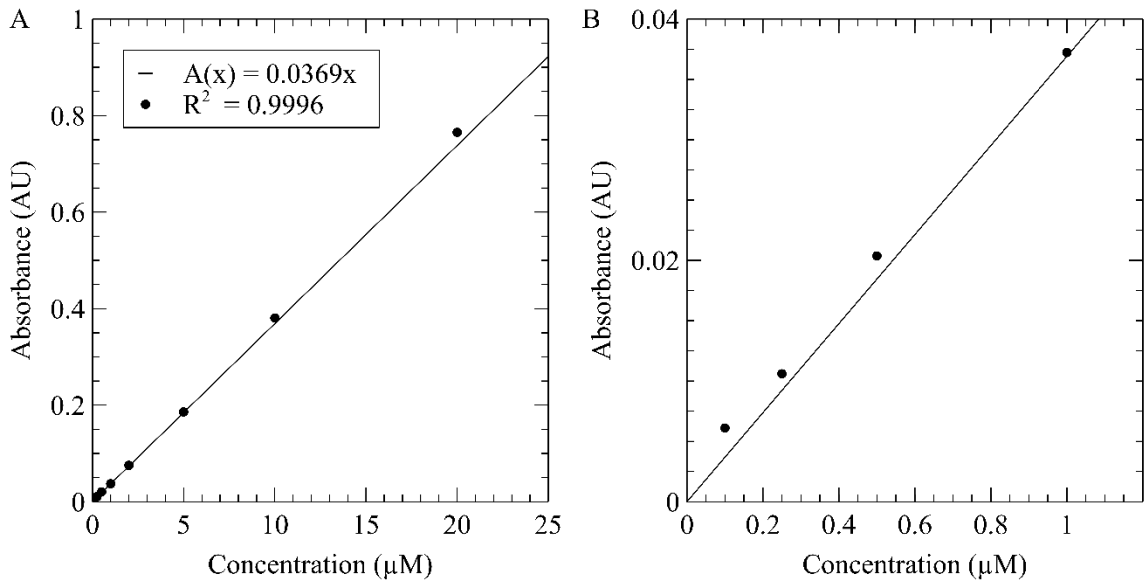

Figure 3: Nitrite calibration curve generated from data collected using the nitrite sensor stack. (Left) shows the full range of absorbance data plotted against concentration while (Right) shows a zoomed in view of the same data showing the first 4 datapoints.

2.3 *In Situ* Data

2.3.1 Data Collection Procedure

The sensor was deployed in the Bedford Basin in Dartmouth, Nova Scotia, Canada. It was suspended from a wharf by a rope causing it to rest at a depth of 0.3 m and 1.6 m underwater depending on the phase of the tidal cycle. A weight was attached to the bottom of the sensor to ensure that the sensor would not float to the surface, as well as to cause the sensor to float in a consistent vertical orientation. It was important for the sensor to be held in this configuration to ensure that the syringes hung down from the bottom of the microfluidic chip thereby any air that entered the syringes would remain at the entrance and be pushed back out rather than floating to the back of the syringe and accumulating there. The sensor, being underwater, could not be consistently communicated with using the wi-fi connection. This necessitated the addition of an

ethernet line that was run from the bottom of the sensor out onto the dock. This line was constructed out of the same type of CAT 6 cable as the power line allowing it to be run through the water without risk of shorting. To avoid the sensor being clogged by environmental debris the sensor required additional filtration. A 10 µm Frit (IDEX Northbrook, Il, USA) was laid over the environmental sample intake port to prevent small debris from entering the microchannels. A larger 3D printed plastic filter was created and affixed to the top of the sensor covering the microfluidic chip entirely. This filter acted to prevent larger debris from entering the intake through its 2 mm diameter holes and provided an additional layer of protection against extraneous light from the sun entering the absorbance cells. A 500 mL reagent bag and a 1 L waste bag were attached loosely to the sensor using a zip tie so that they would not move around too much underwater and possibly tangle their fluid lines. Prior to being fluidically attached to the sensor the reagent bag was primed to remove as much air as possible from the bag.

The sensor was configured such that on start-up the sensor would begin a script that would collect data. The script began by pumping for 3 cycles to flush out the milli-Q water that was used to flush the sensor before use and ensure that the channel would contain an equal mixture of environmental sample and Griess reagent. Next the photodiode outputs were continuously read and saved for both the 25 mm and 10 mm absorbance cell at a rate of 1 Hz. While these photodiode readings were being taken the LEDs were turned on and off such that measurements would alternate between sample measurement and dark reference. The dark references were stored in a separate file so that they could be easily subtracted from the sample measurements later. After 5 min the sample was assumed to have completed reacting and the pumps were run for 3 cycles to flush the completed sample and ready the next one for testing. This procedure allowed the sensor to acquire an absorbance reading approximately every 6 min using 0.75 mL of reagent each time. This allowed the sensor to continue to gather data for up to 67 h before needing to be serviced by adding a new reagent bag.

2.3.2 Environmental Data

Figure 4 shows the data collected during a deployment. 61 measurements were collected over an approximately 6 h long test. Measurements began with the photodiode outputting

3.01 V. Measurements decayed over time until they reached 2.93 V at the 35th measurement. From there, the voltage increased until it reached 3 V by the final measurement. Significant drops in voltage are visible during the 11th and 29th measurements; these appear to drop suddenly during pumping then return to the previous trend after the next pumping cycle. This indicates that the drops are likely the result of small air bubbles or debris entering the channel; then being pumped out before the next reading. Because the sample input was well filtered to prevent debris larger than 0.2 μm in diameter from entering the system, air bubbles are the most likely cause of these drops.

This test was conducted to determine that the sensor would function underwater for extended periods of time while collecting data. Because no blank measurements were taken the data cannot be used to generate absorbance values and, by extension, nitrite values. Continuing work on this sensor, Morgan et al. developed a sensor that incorporates onboard blank samples allowing the sensor to generate accurate concentrations onboard [24]. This sensor was applied to phosphate; however, it used the same reagent-based spectroscopy method. Additionally, to test whether the collected data is correct, environmental samples would need to be taken from the deployment site during the test. These samples would then need to be tested using a known sensor and compared with the readings from the experimental sensor.

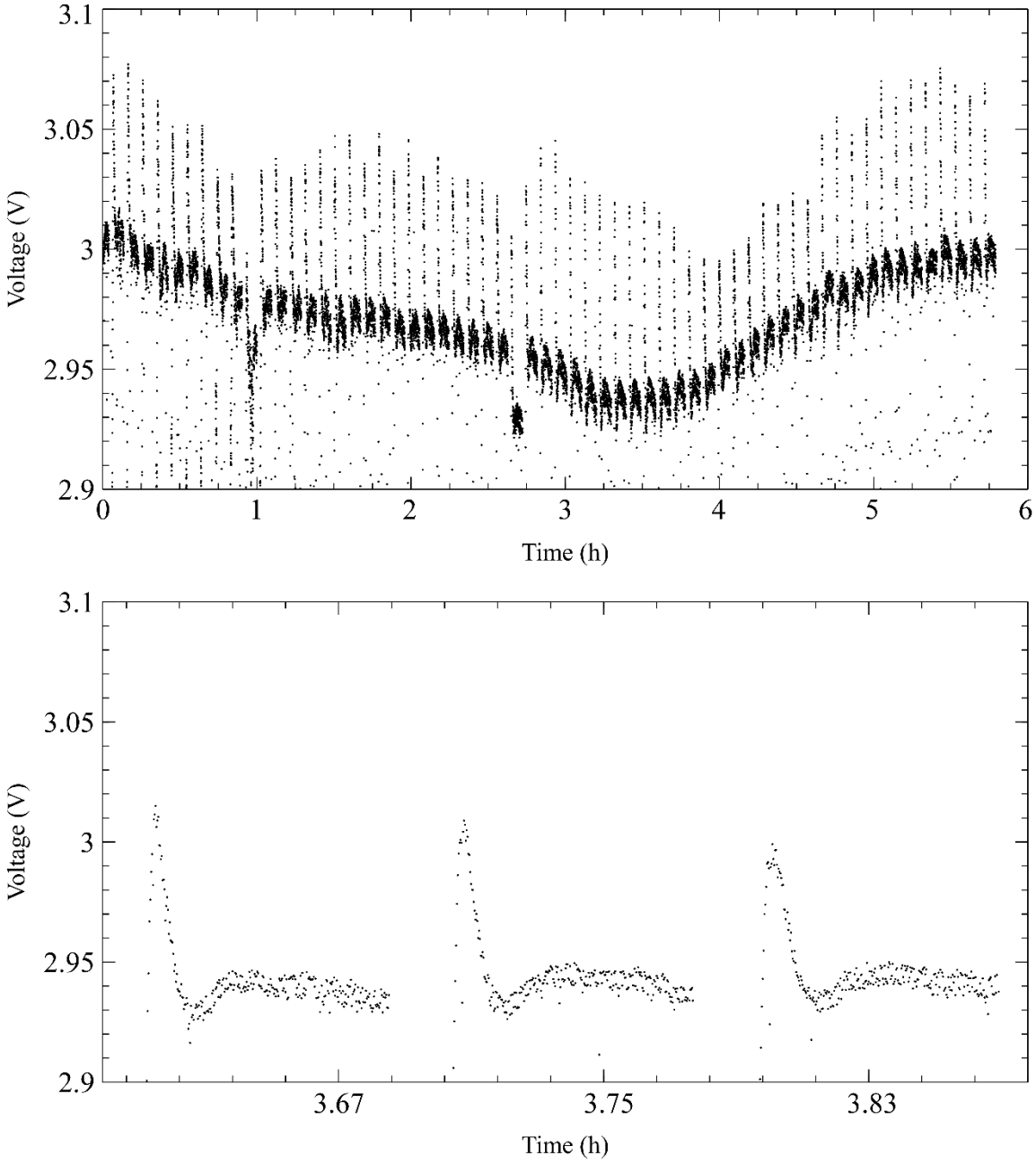

Figure 4: Raw photodiode outputs from an *in situ* deployment. (Top) Voltage over time showing 61 measurements taken during a 6 h deployment. Voltage readings begin at 3.01 V and decay to 2.93 V over the first 3.25 h. The voltage readings stabilize at 2.93 then rise back to 3 V over the last 2.5 h. Two measurements show a significant drop in voltage reading for a single measurement. These are likely the result of bubbles entering the optical channel then being pumped out again before the next measurement. (Bottom) Zoomed in view of three measurements to allow details of each measurement to be visible. Measurements are taken for approximately 5 min while the Griess reaction occurs, and dye develops, then measurements stop for a minute while a new sample is pumped into the optical cell. 0.01 V of noise is visible during each measurement.

2.4 Nitrate Reduction

With the sensor having been demonstrated to effectively sense nitrite concentrations considerations could now be directed toward adapting it to nitrate detection. As mentioned above, to allow nitrate to be detected using the Griess assay the nitrate must first be reduced to nitrite. Two ways of catalyzing this reduction are described here, each having their own strengths and weaknesses.

2.4.1 Cadmium

Cadmium columns are the most common method of reducing nitrate to nitrite. They function by treating a cadmium surface with copper which acts to catalyze the reduction reaction when brought into contact with nitrate. The cadmium column is the gold standard for nitrate reduction because of its rapid and accurate response. However, it is highly toxic making it dangerous to handle and an environmental concern for *in situ* deployments [8], [25]. Additionally, the cadmium column needs to be flushed between uses to remain effective. Yaqoob et al. required 10 mL of 0.1 M NH_4Cl to flush the column between each use [26]. Therefore, if the sensor is meant to acquire thousands of measurements in a single deployment it would require tens of liters to be deployed to support the column reduction step, not counting the copper reconditioning required. Beaton et al. deployed a stop-flow microfluidic and in situ nitrate sensor using the cadmium column reduction and Griess assay approach, reducing the column holdup volume to 80 µL [8]. This sensor is viable for much longer deployments, but the additional fluid handling is still undesirable as it increases the size and complexity of the sensor, and the time per measurement.

2.4.2 Vanadium

Recent efforts have shown that the solid phase cadmium column can be replaced with a reagent reduction based on the less toxic vanadium (III) chloride solution [27]. The vanadium reduction reaction can be combined with the Griess reagent as shown in Figure 5 to both reduce the nitrate to nitrite and form the azo dye without requiring additional fluids on board. The vanadium method is, however, considerably slower than the cadmium reduction, taking multiple hours at room temperature. Schnetger et al. studied the reaction kinetics of the vanadium reduction approach and, if heated from 22 °C to 45

°C, the reaction can be sped up from 390 min to 31 min for achieving over 95 % colour development [27]. As with most reagent-based assays, the reaction kinetics of the vanadium–Griess method occur faster if heated, 10-fold in this case. Although, if the goal is to make an *in situ* instrument, this comes with an energy cost. Performing reagent assays quickly under in situ conditions, such as the vanadium nitrate reduction, will likely require efficient on-chip heating.

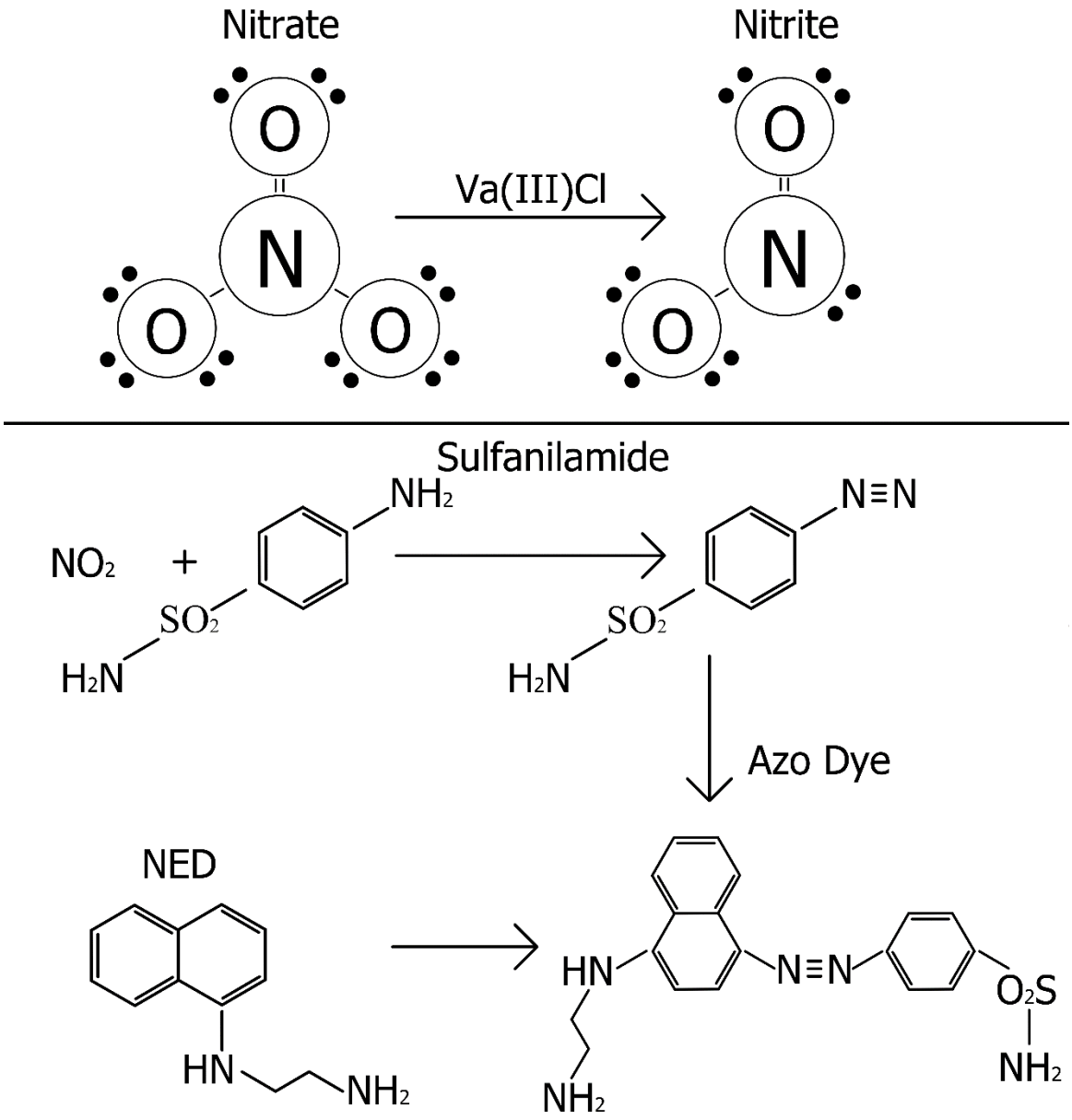

Figure 5: Chemical reactions beginning with nitrate and modified Griess reagent and ultimately forming azo dye [28]. (Top) Nitrate being reduced to nitrite by a chemical reductant, vanadium (III) chloride in this case. (Bottom) The nitrite reacts with the sulfanilamide to create a diazonium salt which combines with the NED (N-(1-aphthyl)ethylenediamine Dihydrochloride) to form an azo dye that is stable and absorbs light best at a wavelength of 540 nm.

2.5 Heating Consideration

Temperature has an effect on the speed at which most reactions occur as well as the rate at which fluids mix [29]. The rates of some reactions, like the reduction of nitrate to nitrite through the use of vanadium (III) chloride, are impacted heavily by the temperature at which they are performed, taking hours at room temperature but only minutes at elevated temperatures around 45 °C. The reaction kinetics are discussed and investigated in greater detail in section 5.2. For FIA systems or stop flow systems that are not stopped long enough for the sample to fully react, it is important for the temperature of the system to be controlled as environmental temperatures change continuously and will change the level of completion the reaction attains for each sample and thereby add significant error to the measured colour or absorbance. The effect of temperature on nitrate reduction reaction kinetics is investigated in more detail in chapter 5.2 where reaction times at room temperature are compared to elevated temperatures in a practical chip. Given that reducing fluid consumption by using microfluidic architectures is another important design concern, heating approaches that couple well to miniaturized channels must be evaluated for efficacy on *in situ* instrumentation.

2.5.1 Lab on Chip Heaters

Microwave

Microwave heaters operate by exposing the sample to an alternating electromagnetic field (EMF) with frequencies in the GHz range. This excites the polar molecules in the sample generating heat through friction between the excited molecules. The amount of electromagnetic energy that will be transferred into heat energy as the EMF passes through a material is dependent on that material's permittivity [30]. By constructing chips using materials with low permittivity, the EMF can be better directed toward heating the fluid sample without wasting energy heating the remainder of the chip. Microwave heating provides fast temperature responses with heating times in the tens of milliseconds [31]. Safely waveguiding the energy and establishing uniform spatial distributions of the EMF in the reactor cavity is challenging. Additionally, it can be challenging to measure temperature in these systems as measurement devices such as thermocouples can affect EMF [32].

Chemical

Chemical reactions can provide temperature control using exothermic reactions; for instance, flowing a 11:1 volumetric mixture of water to sulfuric acid in a parallel channel can generate enough heat to bring a 19 µm by 54 µm channel to 36 °C [33]. However, such approaches require additional reagents to be deployed with the sensor, increasing the size of the system and reducing energy efficiency through necessitating additional pumping [34].

Joule

On-chip resistive heaters are relatively low-cost, require little support equipment, and can be realized in easily customizable shapes. These factors make Joule heating the most common method. Microfabricated heaters are available in a wide array of materials including platinum, doped silicon, and titanium [35]. Using a platinum joule heater, Hoang et al. were able achieve ramp rates of 10 °C per second to perform rapid polymerase chain reaction, cycling temperatures from 60 to 94 °C in a 0.6 µL chamber using only 1 W of power when passively cooled [36]. More simply, isothermal control has been used to accelerate reagent-based assays with resistive heaters. In the case of the nitrate vanadium reduction method, Nightingale et al. performed in situ nitrate measurements with an off-the-shelf polyimide thin-film heater, where the sensor consumed 1.5 W of power with 0.5 W used for heating [5].

2.5.2 Energy Efficiency Considerations for *In Situ* Sensors

While improving reaction kinetics provides clear gains for reagent-based sensors, few studies have focused on the energy efficiency of delivering thermal energy to the microchannel spectroscopy cell. This thesis demonstrates a way to improve the energy efficiency of thermally regulated optical cells by incorporating on-chip insulation. Prior work by Zhao et al. [37] and Dijkstra et al. [38] showed that a suspended microfluidic channel surrounded by an air cavity can be used to efficiently couple thermal energy into a fluid. For example, the system presented by Zhao et al. was able to heat a suspended microfluidic channel to 119.4 °C from room temperature using only 206.9 mW [37]. Such suspended structures have been utilized as flow sensors by either measuring temperature

deviation in the insulated channel [38] or vibrations caused by μ-Coriolis effects [39]. To the best of the authors' knowledge, the use of free-hanging channels has not been applied to performing on-chip optical spectroscopy, where light is coupled into and out of a long suspended and heated microchannel.

CHAPTER 3 DESIGN AND FABRICATION OF A THERMALLY REGULATED MICROFLUIDIC CELL

This chapter will focus on the design of a microfluidic chip for the detection of nitrate. From the considerations laid out in the previous chapters, it was determined that the gold standard reagent-based method would be ideal despite the challenges it poses for *in situ* deployment. The vanadium (III) chloride method for nitrate reduction was chosen to avoid using the highly toxic cadmium column. However, this introduces a further complexity to the design because to allow this reduction to occur quickly it needs to be heated. Joule heating was determined to be an effective method of heating as well as being simple to integrate onto *in situ* sensors. The addition of the heater does add an additional power draw to the sensor which can be a problem for *in situ* sensors that are intended to operate for long periods of time on limited battery energy capacity. Resultantly, reducing the power needs of the heater was an important consideration in the design. This reduction will be accomplished through the addition of insulating air-pockets surrounding the optical channel creating an insulated bridge that can be heated more efficiently than a standard uninsulated microfluidic chip.

3.1 Design Process

Using simulations in COMSOL Multiphysics, designs could be tested and tuned rapidly without having to fully construct new sensors over multiple days. Simulations also allowed the chips to be tested under a more varied set of environmental conditions, like underwater, without requiring full integration onto a submersible sensor. The chips were also modeled as thermal electrical equivalent circuits. The COMSOL simulations were compared with the equivalent circuit models to ensure that the outputs were realistic before physical chips were constructed based off of those simulated designs. Although this thesis presents a logical flow proceeding from COMSOL simulation to thermal equivalent modeling to fabrication, there were a few iterations cycling between simulation, modeling, fabrication, and testing to attain the final design. Some examples of design challenges and how they were overcome are presented here.

Working from a base of the inlaid absorbance cell described in Luy et al. two absorbance cell chips were designed [21]. The primary design concern for the standard chip was how the heater would be integrated on chip. Through simulations it was clear that moving the heater wire closer to the fluid channel reduced the amount of energy required to heat the channel. This made intuitive sense as the temperature in the chip should be hottest at the heater then decay toward room temperature at the edges of the chip. This means that a closer heater does not need to get as hot to attain the same channel temperature. The constraints on how close the heater could be to the channel were primarily manufacturing concerns. The heater needed to be integrated into the chip in a way that would get the heater very close to the channel while maintaining a physical barrier separating the fluid channel from the heater. Additionally, it was important not to add too great a risk of chip failure during the manufacturing process during the added step of heater integration.

The first implementation of the integrated heater was realized by placing a 0.1 mm radius nichrome wire under the bottom inlay during the inlay pressing process such that the wire would run in parallel to the fluid channel 1.1 mm below it. The wire would then emerge from the plate at either end of the inlay and from there could be run out the sides of the chip. This method proved very difficult to manufacture reliably for a number of reasons. Integrating the wire during the inlay pressing step meant that the wire could get in the way during feature milling adding an additional failure risk during this step. Additionally, the thin wire did not maintain its shape well during the pressing which lead to inconsistent heating in the channel.

A second design was realized in which an additional 400 µm by 400 µm heater channel was milled next to the fluid channel to house a 0.3 mm diameter nichrome wire. The thicker wire allowed the heater to better maintain its shape and keep the temperature more consistent along the length of the fluid channel. Additionally, the heater wire could now be placed into the chip after features were milled into the inlaid plates. This design also provided better control over the distance between the heater and the fluid channel with the major constraining factor now becoming maintaining the structural integrity of the PMMA between the heater and fluid channel. Through this design a heater was integrated on-chip at a distance of 650 µm from the channel.

For the insulated design the primary concern was the size and shape of the insulating air-pockets. The size of the air pockets was important with larger air pockets giving better thermal resistance between the heated section of the chip and the environment. The shape of the air pockets was also important; ideally the channel and heater would be as fully surrounded by the air pocket as possible while still being fluidically connected to both the fluid input and output. To realize this a suspended bridge design was realized that allowed the channel to be surrounded on the four long sides by the air pockets while still being securely attached at either end of the fluid channel. Originally the air pocket was 25 mm long, the same length of the channel, but this led to the channel being much better insulated at the centre than at the ends of the channel causing the temperature to be inconsistent. This was improved by making the air pocket 40 mm long, overshooting the end of the absorbance channel by 7.5 mm on each side.

The other major constraint on the air-pocket was manufacturability. Originally the design used only two 6 mm thick PMMA plates. This made it challenging to create the suspended bridge using the mill. To achieve this, special inlays were made in the shape of the suspended bridge; however these inlays warped significantly when pressed into the clear PMMA and were not viable. To achieve the suspended bridge using the rapid prototyping materials available in the lab the bridge would need to be milled out after the inlays were pressed and the features milled onto the plates. To do this an extra “cap” plate was added to the top and bottom of the design. This design allowed the air pocket to be milled into the middle two plates from the outsides after the middle plates were pressed together; then the holes in the top and bottom could be covered by the new cap plates to create the fully contained air pocket. To avoid warping the cap plates or possibly crushing the existing microchannels the cap plates were not attached to the middle plates using the press. They were instead attached to the middle plates using screws inserted into holes milled at the corners that passed through all four layers. During optical testing light was not passing through the insulated chip well; this was theorized to be the result of the light having to pass through several PMMA to air and air to PMMA interfaces including some PMMA surfaces that were rough from milling. To account for this, 3.4 mm diameter columns were left in the clear PMMA, connecting the suspended bridge to the top of the chip where light entered and exited the optical cell. This brought the insulated chip’s

optics in line with the standard chip's at the cost of creating two small thermal paths across the insulation that were not ultimately accounted for in simulation.

Having overcome these fabrication challenges, an insulated absorbance cell that was manufacturable using available rapid prototyping methods was created as well as a standard uninsulated version to compare it against. The fabrication constraints permitted rapid parametric evaluation using simulation to arrive at a thermally/energetically optimal design. Having arrived at final designs for each chip their parameters and simulated performance will be described in greater detail in the subsequent sections of this chapter.

3.2 A Novel Insulated Air-Pocket Absorbance Cell

Figure 6 shows the microfluidic optical absorbance cell with integrated heaters in both the standard and insulated configurations. The design was based on the "inlaid" optical cell approach first implemented by Luy et al. [18]. Figure 6A shows how the black polymethyl methacrylate (PMMA) is embedded within clear PMMA and depicts the light passing through the microchannel optical cell to make colourimetric measurements. The dark PMMA surrounding the optical channel prevents extraneous light from entering the channel and interfering with measurements. The light from the light-emitting diode (LED) shines down through a clear hole in the dark PMMA, reflects off of a 45° prism, passes through the 25 mm optical channel, reflects off of a second 45° prism, and finally, reaches the photodiode. Figure 6B compares the standard and insulated on-chip resistive heater designs using a 3D rendering, with the top and bottom halves of the chip separated to highlight the internal details of the chip. The heater, fluid channel, fluid input, and fluid output are labeled on the standard chip. Figure 6C,D provides cross-sectional views of the standard and insulated designs. Figure 6C illustrates the standard configuration of the black PMMA inlayed in clear PMMA and fluid channel, as well as the heater wire. Figure 6D shows the integral air pockets around the optical absorbance cell, forming an insulated bridge design. The approach conserves energy by increasing the thermal resistance to the local environment. Placing the air pockets close to the sensing channel permits rapid thermal control and minimizes thermal mass. The inlaid absorbance cell augmented with

integral insulated heating allows for low volume, low power, thermal regulation, and on-chip colourimetric spectroscopy.

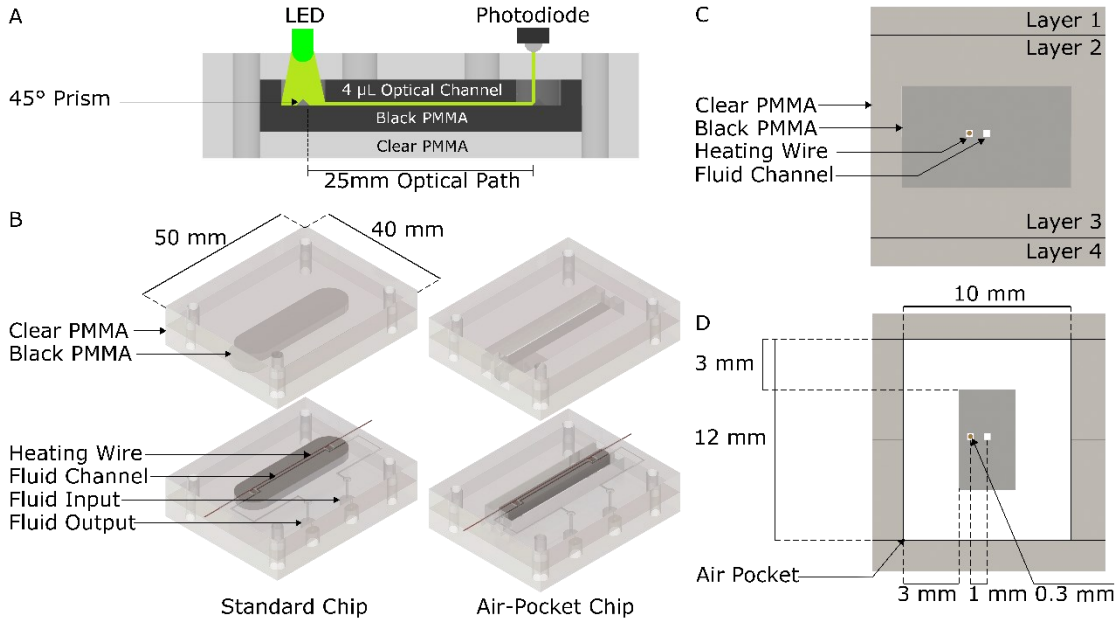

Figure 6: (A) Cross-section of the inlaid absorbance cell, identifying the light-emitting diode (LED) light source, the reflecting prisms, the optical path, and the hybrid black and clear polymethyl methacrylate (PMMA) chip design. (B) The 3D rendering of the chip with the top and bottom halves of the chip separated to show its internal features for both the standard and insulating air pocket designs. A nichrome wire inserted beside the channel provides thermal regulation of the absorbance cell. (C) Cross-section of the standard chip design, showing the layout of the wire and channel in the inlay. (D) Cross-section of the insulated chip design, showing air pockets added around the optical cell to create an integral cavity and increase thermal resistance to the environment.

3.3 COMSOL Simulations

Figure 7 compares the simulated thermal response of the standard and insulated optical cell designs with a temperature setpoint of 35 °C in the fluid channel and boundary conditions of convection in air at 20 °C. The simulations were performed in COMSOL using the electric currents, heat transfer in solids and fluids, and electromagnetic heating Multiphysics functions. Simulations were performed on a computer with 32 Gigabytes of RAM and a 12 core Ryzen 9 3900X processor allowing for computation times under 10 s.

The material dimensions and parameters used for these simulations can be found in Appendix A.

The cross sections of the center of both chips are shown in Figure 7A,B to illustrate the heat distribution under steady state conditions. The scale bar, shown to the right, covers the temperature range from the boundary conditions of room temperature (Blue - 20 °C) to the maximum in this instance near the heater (Red - 45 °C). The inset shown in the top right corner of Figure 7A,B represents a magnified view of the center of each chip. In the insets, the square geometry is the channel created from micro-milling and the circular geometry is the heater wire. As expected, the highest temperature in both chips is the heater and the temperature decreases in both chips toward the edges or boundary conditions. When the center of the microfluidic channel is set to 35 °C, the nichrome wire heater must be set to 37.8 °C in the insulated chip, whereas the standard chip wire must be set to 41.7 °C to account for the lack of insulation.

Driving the heater to a higher temperature requires more current or power and, in the simulation, the air pocket design reduces the power required to maintain the channel temperature at 35 °C from 290 mW to 117 mW. Similarly, with a setpoint of 45 °C, the power is reduced from 490 mW to 200 mW, and at 55 °C, from 695 mW to 283 mW. These power setpoints were determined iteratively by varying the current input until the desired temperature setpoint was reached at the center of the fluid channel.

The reductions in power required from the standard to the insulated chip at 35 °C, 45 °C, and 55 °C were 59.6, 59.2, and 59.3 %, respectively. This represents a significant reduction in power usage for the range of targeted temperature setpoints suitable for reagent-based assays. The above power values required for the heater design are in line with Martinez-Quijada et al., who showed clean-room fabricated thin-film heaters that consumed 1130 mW to elevate a 1 cm chip to 95 °C in 22 °C ambient air [40]. When the insulated heater design is driven to 95 °C, the simulated power consumption is comparable at 900 mW. Therefore, this design shows comparable performance to cleanroom-fabricated devices but is implemented with more readily available rapid prototyping approaches available at Dalhousie University.

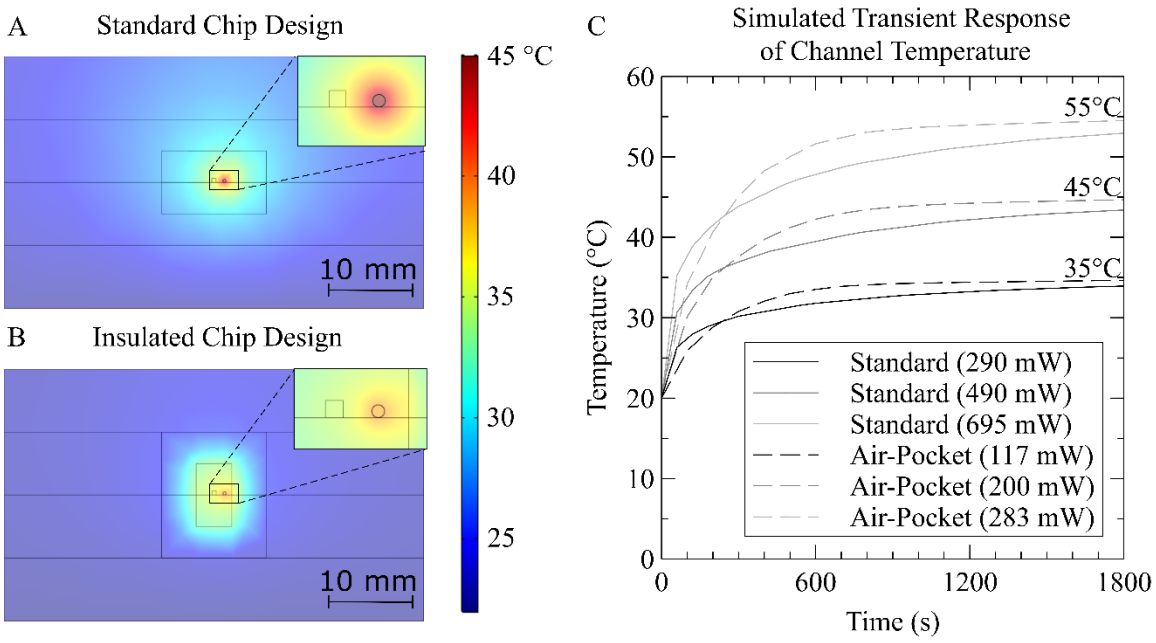

Figure 7: (A) Simulated cross-sectional heat distribution in the chip at steady-state conditions without insulating air pockets. The temperature setpoint is 35 °C at the center of the microchannel and required 0.618 A supplied to the heater, which itself attained a temperature of 41.7 °C. (B) Simulated cross-sectional heat distribution in the chip at steady-state conditions with insulating air pockets. The same 35 °C channel setpoint required 0.393 A supplied to the heater, with the heater reaching 37.8 °C. (C) Transient response of the simulated chip without air pockets (solid lines) and with air pockets (dashed lines) for the first 30 min, showing improved responsivity and energy efficiency of the insulated design. Simulations details described in text.

The heat distribution across the fluid channel cross-section in the insulated chip is also more uniform than in the standard chip. In the case of a fluid channel setpoint of 35 °C, where the entire chip is immersed in air at 20 °C, there is a change in temperature of 1.06 °C from one side of the channel to the other in the standard chip, and 0.55 °C in the insulated chip. These temperature differences were determined by comparing the temperatures at the closest and furthest point along the x axis in the center of the channel along the y and z axis. The thermal gradient across the fluid channel cross-section arises from the thermal resistances to the boundary conditions; please see Section 3.5 on the electrical equivalence thermal modelling of the system as well as Table 1 for the material properties used to calculate the thermal impedances. In the standard chip, the temperature drops off gradually over the full distance between the heater and the chip boundary/edge,

whereas in the insulated chip, the elevated temperature is confined to the optical cell with a steep gradient across the air pockets. A more uniform temperature profile in the insulated design is more advantageous as it will lead to more consistent reaction kinetics with reagent-based analyzers.

Figure 7C compares the simulated transient response of both chips. The simulated chips began at 20 °C and were heated to microchannel temperature setpoints of 35 °C, 45 °C, and 55 °C using constant currents of 0.618 A, 0.803 A, and 0.956 A for the standard chip and 0.393 A, 0.513 A, and 0.610 A for the insulated chip, respectively. For the first 250 s, the center of the fluid channel has a higher temperature in the standard chip than in the insulated chip. This is an expected result, as the heater in the insulated chip is driven at a lower input power, taking longer to heat the immediate thermal mass of the PMMA plastic. This causes the temperature of the fluid to rise slower during the initial heating phase. However, the air cavity in the insulated design introduces a significant thermal resistance, improving the thermal energy retention, allowing the temperature to overtake the standard design at approximately 5 min. The standard chip reached 95 % of the temperature setpoint in 33 min, while the insulated chip required only 17 min to plateau.

The faster transient response of the insulated design can further improve its energy efficiency, as less time is required to attain steady-state temperature. To achieve steady state, the standard chip required 33 min and the insulated chip required 17 min, with both chips then holding for an additional 10 min of reaction time. Typical reagent-based colourimetric analyzers that perform stop flow schemes allow colour development to occur over at least 2 min, though often waiting longer [8], [41]. Faster temperature response is particularly advantageous when an *in situ* sensor is acquiring measurements infrequently, where the sensor will be put into an unheated sleep mode most of the time. When considering the heating up times of 33 min in the standard chip and 17 min in the insulated chip plus the hold time of ten minutes, and that energy is the product of power and time the standard chip requires 0.75 kJ, 1.26 kJ, or 1.79 kJ for infrequent measurements to raise the temperature from 20 °C to 35 °C, 45 °C, or 55 °C in air, respectively. Similarly, the insulated chip requires 0.19 kJ, 0.32 kJ, or 0.46 kJ for the

same temperatures, respectively. For each of the temperature setpoints, this is a 74.6, 74.4, 74.4 % reduction in the energy required, respectively.

3.4 Simulation at 4 °C and Submersed in Water

While Figure 7 was simulated at 20 °C ambient in air, this heater is intended for in situ deployments in waters. Figure 8 shows the simulated results for the identical chip designs with the boundary conditions being convection in water at 4 °C. The 4 °C was chosen arbitrarily to simulate the cold temperatures found in deep water environments; however, temperatures can be near freezing in many marine environments. The Figure 8 simulations are similar to those shown in Figure 7, where the air pockets caused the heat distribution to change significantly. The temperature in both chips is highest at the heater and decays as it approaches the edges of the chip. In the standard chip, this decay was gradual throughout the chip while in the insulated chip the temperature drop occurred primarily within the air pocket. The simulation in 4 °C seawater differs from the simulation in 20 °C air primarily in the amount of power that was required to heat the chip and the temperature that the heater had to reach to achieve the desired temperatures. To achieve the channel temperature setpoints of 35 °C, 45 °C, and 55°C in oceanic conditions the standard chip required 0.727 W, 0.965 W, and 1.20 W while the insulated chip required 0.255 W, 0.340 W, and 0.428 W. This is a significant increase in required power over the simulation of the chip in 20 °C air that required 2.90 W, 0.490 W, and 0.695 W in the standard chip and 0.117 W, 0.200 W, and 0.283 W in the insulated chip. This increase in required power is the expected result of having to maintain a 16 °C higher difference between channel temperature and ambient temperature. Additionally, the thermal conductivity of water (0.6 W/m*K) is much higher than the thermal conductivity of air (0.026 W/m*K) which leads to more energy being lost to convection in water [42]. The efficiency improvement from the added insulation reduced the power required to heat the chip by 65.0 %, 64.58 %, and 64.5 % under oceanic conditions. Similar to the simulations under benchtop conditions, when heating from 4 °C to 35 °C, 45 °C, or 55 °C in water, then waiting 10 min at that temperature; the faster transient response of the insulated design provides additional energy savings. The energy reduction

from the standard chip to the insulated chip is 1.88 kJ down to 0.41 kJ (4 °C to 35 °C), from 2.49 kJ down to 0.55 kJ (4 °C to 45 °C), and from 3.11 kJ down to 0.69 kJ (4 °C to 55 °C). For each of the temperature setpoints, this is a 78.0, 77.9, and 77.7 % reduction in the energy required, respectively.

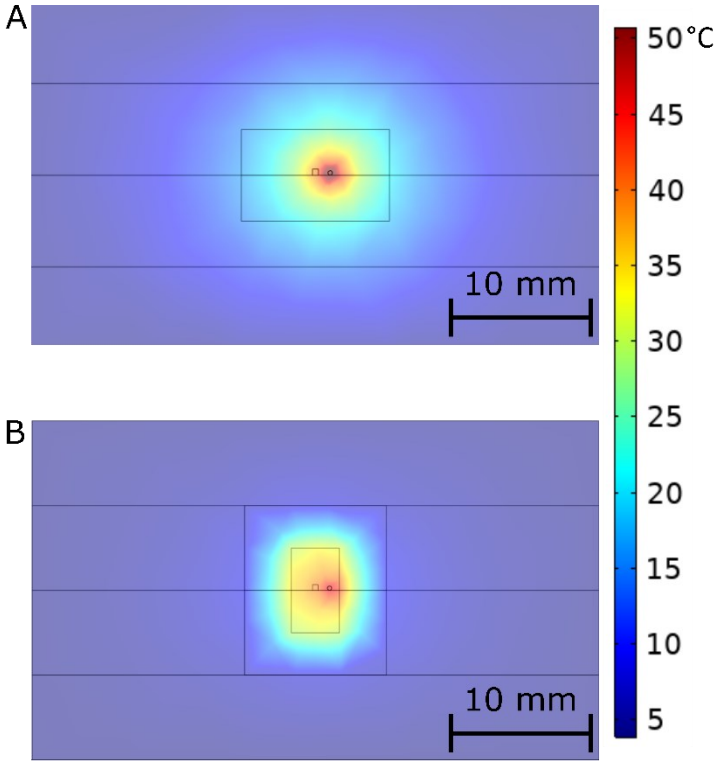

Figure 8: (A) Simulated cross-sectional heat distribution for the standard chip submerged in 4 °C water. The temperature setpoint is 35 °C at the center of the fluid channel and required 0.978 A supplied to the heater, which itself attained a temperature of 50.8 °C. (B) Simulated cross-sectional heat distribution in the chip at steady-state conditions with insulating air pockets surrounding the fluid channel and heater. The same 35 °C channel setpoint required 0.579 A supplied to the heater, with the heater reaching 40.7 °C.

The increase in power required is accompanied by an increase in heater temperature for the same materials and geometries. For the 3 temperature setpoints, the simulation in 4 °C seawater required heater wire temperatures of 50.8 °C, 65.8 °C, and 80.7 °C in the standard chip and 40.7 °C, 52.7 °C, and 64.6 °C in the insulated chip. This is higher than the heater temperatures when the system is simulated in air at 20 °C of 41.7

°C, 56.3 °C, and 70.9 °C in the standard chip and 37.8 °C, 50.1 °C, and 62.0 °C in the insulated chip. While the heater temperatures are higher in the simulations performed in 4 °C seawater, the temperatures do not approach the glass transition temperature of PMMA of 100 °C to 130 °C so this chip material would still function under these conditions [43].

3.5 Thermal Electrical Equivalent Model

Figure 9 shows the standard and insulated chips modeled as a set of equivalent thermal resistances and capacitances, following the N-stage RC transmission-line equivalent circuit model of the heat-diffusion equation covered by Bruus [44]. This model is an infinite parallel-plate approximation and as such under-represents the true 3-dimensional heat transfer problem. Additionally, the model assumes materials are homogeneous and that heat transfer is proceeding in a single direction. For this reason, identical transient and steady-state voltages compared to those reported by COMSOL or those found in physical experiments are unlikely, but the orders of magnitude in calculations should be similar. In a thermal equivalent circuit model, the temperature is modeled as voltage or potential difference, and each material layer of the microfluidic chip can be modeled as a thermal resistor and thermal capacitor to capture heat transfer through the device [44]. Equation 3.1 shows the thermal resistance (R_{th}) which is defined as the height (h) of the layer divided by the layer's surface area (A) and thermal conductivity (k) [44]. Equation 3.2 shows the thermal capacitance (C_{th}) which is defined as the height (h) of the layer multiplied by its surface area (A), and its material's density (ρ), and specific heat capacity (c_p) [44]. Equation 3.3 shows the heat lost to *convection* in the air around the chip which is calculated as a resistance (R_{con}) defined as 1 divided by the heat transfer coefficient (K) of air (7.5 W m^{-2} K^{-1}) and the area of the surface of the chip (A) [44]. The thermal conductivity, density, and specific heat capacity for PMMA, water, and air are listed in Table 1. Tables 2 and 3 list the height, area, and material of each section as well as the resulting thermal resistances and capacitances. With these resistance and capacitance values, the microfluidic designs can be modeled as electrical equivalent circuits.

$$R_{th} = \frac{h}{kA} \tag{3.1}$$

$$C_{th} = \frac{1}{2} hA\rho c_p \tag{3.2}$$

$$R_{Con} = \frac{1}{KA} \tag{3.3}$$

Table 1 Parameters used to determine thermal resistance and capacitance for the electrical equivalent model.

	k (W/m*K)	ρ (kg/m^3)	c_p (J/K)	Source
PMMA	0.17	1200	1400	[44]
Water	0.6	1000	4200	[44]
Air	0.026	1.2	1000	[45]

Table 2 Parameters of the standard chip model.

Material	h (mm)	A (mm^2)	R_{th} (Ω)	C_{th} (F)
PMMA	19.8	50x24	97	40
Water	0.4	25x0.4	66.7	0.0168
PMMA	0.65	50x24	3.19	1.31

Table 3 Parameters of the insulated chip model.

Material	h (mm)	A (mm^2)	R (Ω)	C (F)
PMMA	15	50x24	73.5	15.1
Air	3	40x12	240.4	0.00176
PMMA	1.8	50x6	35.3	0.907
Water	0.4	25x0.4	66.7	0.0168
PMMA	0.65	50x6	12.7	0.328

The magnitude of the voltage source, which represents the heater, is set to the difference between the temperature at the heater and the ambient temperature of the environment. In the COMSOL simulations outlined in Figure 7 the temperature at the heater required to reach 35 °C in the microfluidic channel is 41.7 °C in the standard chip and 37.8 °C in the insulated chip. When the voltage, which is analogous to temperature,

in the equivalent circuit is set to these values the channel temperature is 38.9 °C in the standard chip and 36.3 °C in the insulated chip. These values are close to the expected 35 °C temperature and indicate that the equivalent circuit and COMSOL simulations are in reasonable agreement about the expected channel temperatures.

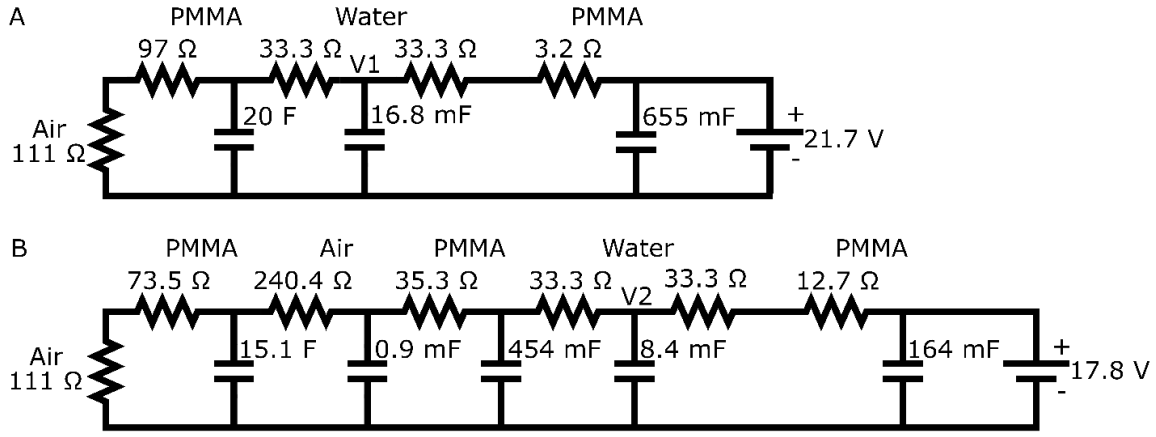

Figure 9: (A) Thermal equivalent circuit of the Standard chip. The heat originating at the heater wire must pass through PMMA to reach the water in the microfluidic channel then more PMMA to reach the outside of the chip. The point at the center of the channel where the voltage is measured is marked with V1. (B) Thermal equivalent circuit of the insulated chip. This circuit is similar to the standard chip circuit with the PMMA broken up by the addition of a more thermally resistant air pocket. The point at the center of the channel where the voltage is measured is marked with V2. In both chips, ground is defined as room temperature (20 °C) and the potential differences across the voltage sources are the difference between the elevated wire temperature and ambient room temperature.

The transient thermal response of the microfluidic design was also simulated using circuit equivalence methods as displayed in Figure 10. This transient response is compared to the transient response from the simulated chip in Section 3.3. In the equivalent circuit, the time it takes for the temperature in the microfluidic channel to reach 95 % of its final temperature is 38 min for the standard chip and 5 min for the insulated chip. The transient response of the chips in the COMSOL simulations is 33 min for the standard chip and 17 min for the insulated chip to reach the same 95 % completion threshold. While the heating time of the standard chip is very similar between simulation and circuit equivalent, the insulated chip was much less so. This is likely due to incorrect

modelling of the air pocket as a conductive element in the circuit equivalent model, which unlike the COMSOL simulations does not appropriately capture the convection that is occurring within the air pocket. Despite the difference in heating time, the circuit equivalent (1D plane) shows the same shape as the finite element method of COMSOL (3D) for the transient response. The insulated chip heats much faster than the standard chip and levels off quickly while the standard chip heats more gradually coming to a slower plateau. From these similarities and the similar temperature steady states the simulated results were determined to be reasonable.

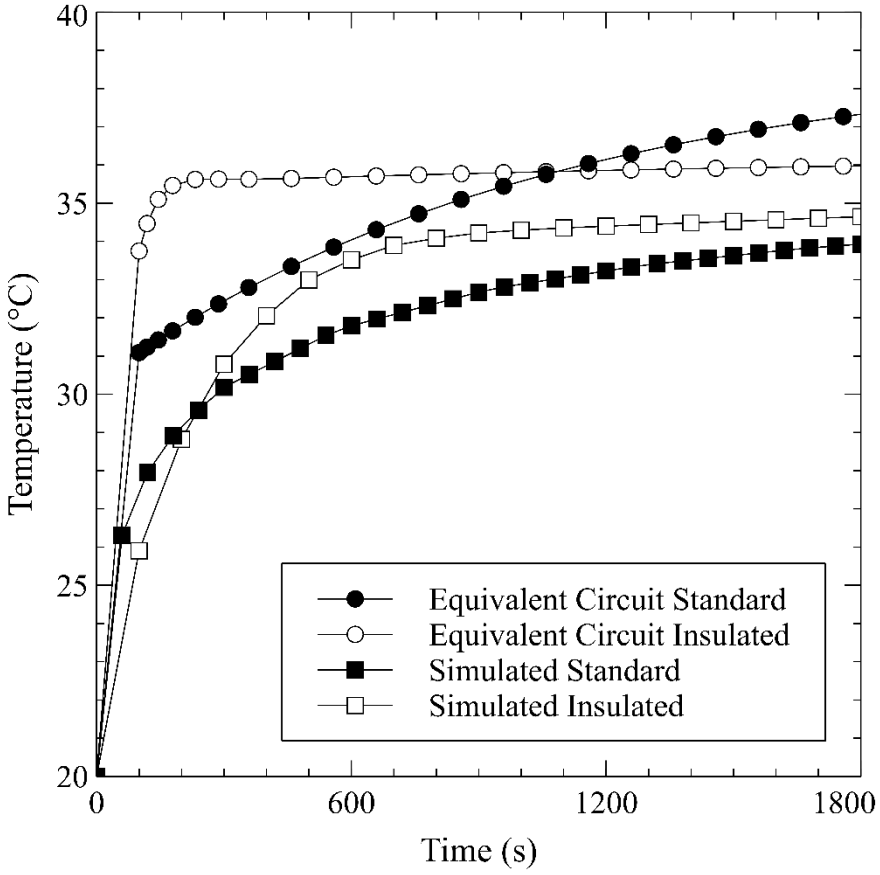

Figure 10: The transient temperature response of the standard chip (solid) and insulated chip (hollow) are compared over the first 30 minutes rising from room temperature (20 °C). Additionally, the transient responses simulated in COMSOL (squares) are compared to the transient responses from the circuit equivalent model (circles). A similar pattern between the COMSOL simulations and the circuit equivalent model is evident; the standard chip gradually approaches its steady state temperature and the insulated chip heats up faster, then levels off more sharply towards its steady state temperature.

CHAPTER 4 FABRICATION AND VERIFICATION

Having been simulated extensively, the chips were constructed physically. This chapter describes the procedure used to create the chips as well as how the chips were tested to verify the simulations. The simulated chips were compared to the experimental chips to further tune the predictive capability and completeness of my simulations during the design process.

4.1 Chip Fabrication

The design of the thermally isolated microfluidic absorbance cell was made from four substrates of 6 mm-thick PMMA (0A000, Acrylite, Sanford, ME, USA) using a modified approach to what was described by Luy et al. [21]. Modifications to the published procedure were made to incorporate a heating element embedded between the layers and to make integral air pockets. First, an LPKF S103 micro-mill (LPKF, Garbsen, Germany) was used to mill recesses into the middle two clear PMMA substrates to allow black PMMA (9M001, Acrylite, Sanford, ME, USA) to be inlaid into them. The black PMMA was cut into the shape of the recessed cavities in the clear PMMA using a 50-watt Epilog Mini laser cutter (Epilog, Golden, CO, USA). Both the clear and black PMMA were exposed to chloroform to soften the plastic and then, the black PMMA was pressed into the clear PMMA base using an LPKF Multipress II for 3 h at 116 °C and 43 N cm^{-2}. The inlaid optical cell ensured that the final absorbance measurements were conducted on the fluid alone, preventing extraneous or scattered light from entering the optical channel. The inlaid substrate (black and clear PMMA interwoven) was then leveled by shaving 200 µm off from the top of the sheet using an LPKF micro-mill. This was carried out to ensure a smooth surface with substrate thickness uniformity and a channel depth accuracy of less than 10 µm. Microchannel features were cut into the leveled inlaid PMMA with the LPKF S103 micro-mill; nominal fluid channel dimensions were 400 µm deep and 400 µm wide. The individual chip plates were then cut out with the Epilog Mini Laser. Both interior plates (labelled layers 2 and 3 in Figure 6C) were then sanded and scrubbed to ensure the surfaces to be pressed together were both clean and deburred. Next, these middle two substrates were exposed to chloroform vapor for 45 s to soften

them for bonding. A 300 µm diameter nichrome-80 wire was placed into the designated pre-cut channel, then the two substrates were aligned with dowels and hand-pressed together. The combined substrates were placed in the automated LPKF Multipress II for 135 min at 85 °C and 625 N cm^{-2} to complete the bond. After the middle two plates were pressed, air pockets were milled into the chip around the optical absorbance channel to create a bridge containing the optical channel and heater wire, as shown in Figure 6B,D. Finally, features were milled into the top and bottom plates using the LPKF S103 micro-mill and then were cut out using the Epilog Mini Laser. The layer 1 and 4 plates were screwed onto the top and bottom of the chip, thereby enclosing the air around the bridge and creating an air pocket. To create the standard chip, the procedure was the same, except air pockets were not created around the optical channel and heating wire.

4.2 Verification with Experimental Chips

Figure 11 demonstrates surface thermal characterization of the microfluidic devices by showing a top-down view of the standard and insulated chips, both in the simulation and as measured experimentally. Figure 11A shows the simulated results with the standard chip at the top of the image and the insulated chip at the bottom of the image. Crosshairs were placed at both the center and bottom left-hand corner of both chips. The crosshairs were labeled with the readings at their centers and were placed such that they would record the maximum and minimum temperatures of the chip. To confirm the accuracy of the simulations, the surface temperature was recorded using FLIR ONE Pro (FLIR, Wilsonville, OR, USA) infrared camera with an accuracy of 2 °C [46]. The acquired thermal image, displayed in Figure 11B, shows the two built designs: the standard chip and the insulated chip.

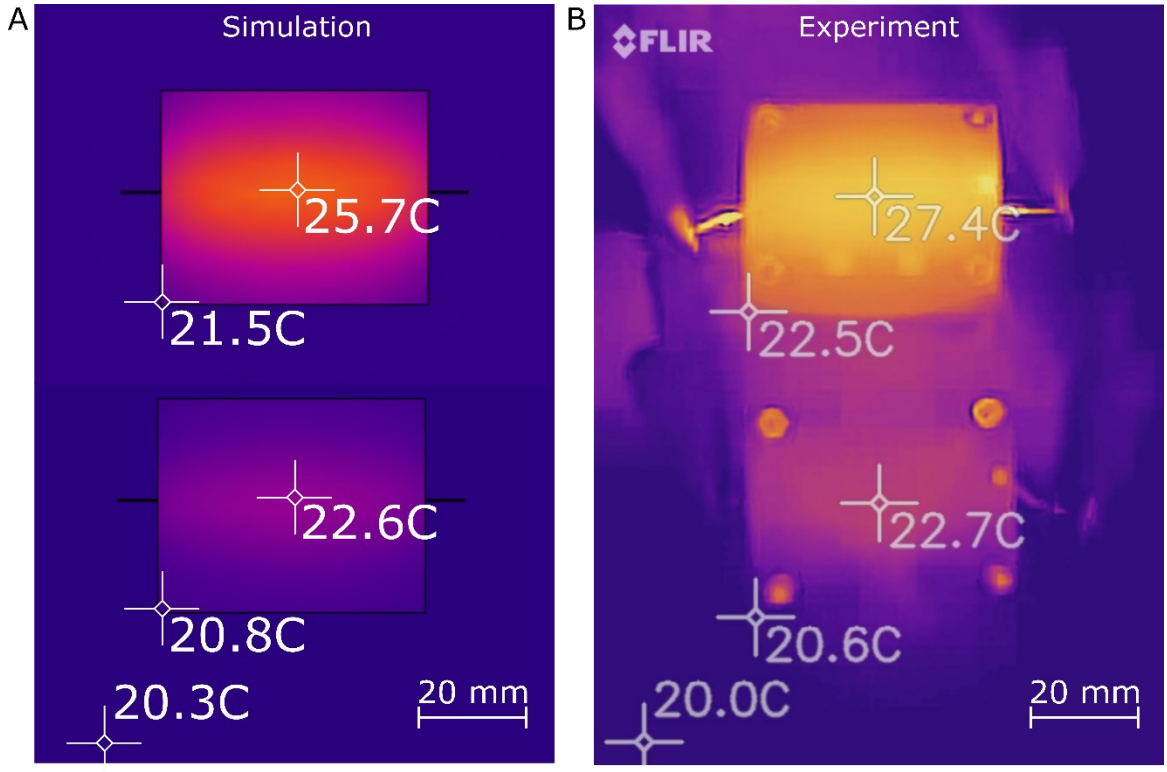

Figure 11: (A) Simulated top-down heat distribution of the microfluidic chips. The top rectangle represents the standard chip, and the bottom rectangle represents the insulated chip; both channel temperatures were set to 35 °C. The crosshairs represent the chip surface temperature at the location in the center of the crosshair; for example, the center of the standard chip is 25.7 °C, whereas the center of the insulated chip is 22.6 °C. (B) Experimental top-down thermal image of the heat distributions for the standard (top) and insulated (bottom) microfluidic chips, confirming simulations within the uncertainty of the measurements [38].

As with Figure 11A, Figure 11B shows the standard chip at the top and the insulated chip on the bottom with the temperatures at the center and bottom left corner marked with crosshairs. In both the simulation and experiment, the nichrome wire heater was given 0.618 A in the standard chip and 0.393 A in the insulated chip. The current values were chosen to bring the fluid channel from 20 °C to 35 °C as predicted by the simulation. The standard chip's temperature ranges from 21.5 °C to 25.7 °C in the simulation and 22.5 °C to 27.4 °C in the experiment. The experimental temperatures for the standard chip as recorded by the FLIR one camera are higher than the simulations by 1.0 °C ±2 °C at the lower left corner and 1.7 °C ±2 °C at the center. The surface

temperature of the insulated chip ranged from 20.8 °C to 22.6 °C in the simulation and 20.6 °C to 22.7 °C in the experiment. The insulated chip showed excellent agreement with the simulations, with a 0.2 °C ±2 °C difference at the corner and 0.1 °C ±2 °C at the center. The differences noted are within the ±2 °C accuracy of the FLIR one camera, indicating that simulations and experimental results had comparable surface heat distributions [46].

The surface of the insulated chip was cooler than the surface of the standard chip by 3.1 °C in the simulation and 4.7 °C in the experiment at the center of each chip. This result was expected since the insulated chip requires less power to maintain a temperature of 35 °C in its fluid channel in steady state conditions. Therefore, less heat was dissipated on the surface. These modeling efforts will enable future optimization as they reflect the experimental observations very well.

Figure 12 shows the measured transient heat response of both the standard and insulated chips at three temperature setpoints. In the case of the standard chip with a setpoint of 35 °C (black lines), the heater wire in the standard chip was driven at a constant current of 0.65 A and the temperature at the center of its fluid channel was monitored using a k-type thermocouple (TP870, Extech, Boston, MA, USA) for 30 min. In total, 600 temperature measurements were acquired over the duration of the test. The temperature started at 20 °C, or room temperature, and rose to 35 °C, beginning to plateau after 10 min. For the other two temperature setpoints, 0.88 A and 1.08 A were used, and correspondingly, the temperature at the center of the same chip was observed to rise from 20 °C to 45 °C (dark grey lines), and from 20 °C to 55 °C (light grey lines). The same procedure was repeated for the insulated chip, where 0.51 A, 0.68 A, and 0.82 A were used to evaluate the transient response for the same three temperature setpoints.

The devices tested in Figure 12 were different than those of Figures 9 and 11, in that a thermocouple port was added as described in material and methods to monitor the transient response of the channel temperature. It was empirically determined that to reach the three temperature setpoints of 35 °C, 45 °C, and 55 °C, the standard chip required input powers of 325 ± 5 mW, 596 ± 8 mW, and 898 ± 12 mW, respectively. Similarly, to reach the same temperatures, the insulated chip required 199 ± 3 mW, 357 ± 5 mW, and

524 ± 7 mW, respectively. The error in power was calculated from the combined measurement error values for current and resistance measurements given in the multimeter (5491B, B&K Precision, Yorba Linda, CA, USA) datasheet. The data from these experiments show that insulation reduced power consumption by 38.9 % for the 35 °C temperature setpoint, by 40.0 % for the 45 °C setpoint, and by 41.6 % for the 55 °C setpoint.

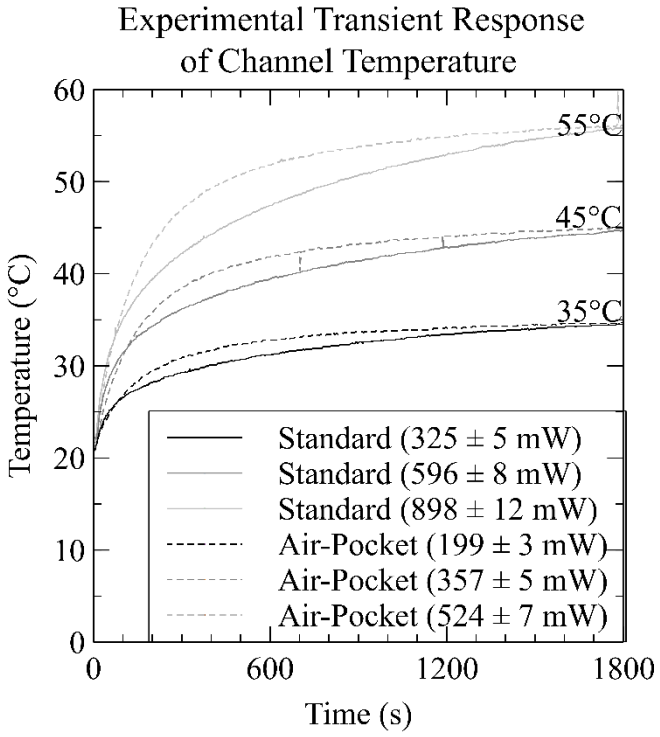

Figure 12: Experimental comparison of the transient responses of the fabricated microfluidic devices. The standard chip (solid lines) and the insulated chip (dashed lines) were evaluated at 3 temperature setpoints of 35 °C, 45 °C, and 55 °C. The air pockets reduced power consumption by 38.9% for the 35 °C temperature setpoint, of 40.0% for the 45 °C, and 41.6% for the 55 °C.

Figure 13 compares the experimental results in Figure 12 to the simulations of Figure 9. The power required to reach 35 °C, 45 °C, and 55 °C was 12.1 %, 21.7 %, and 29.3 % higher in the experiment than in simulations for the standard chip. Similarly, the power required was 69.5 %, 78.7 % and 85.5 % higher in the experiment than in

simulations for the insulated chip. Therefore, instead of a 60 % average reduction in energy as predicted by simulations when implementing the air pocket design, only an approximately 40 % average power reduction was observed. This discrepancy in energy reduction can be attributed to two differences between the simulation and experiment. First, the initial simulations did not include the added thermal mass of the thermocouple. Second, to bring the thermocouple into communication with the channel, the insulating air pockets were broken, thus permitting air to pass through the thermocouple port allowing for additional heat dissipation, and third the optical connections added to the insulated design also allow some heat to transfer past the air-pocket.

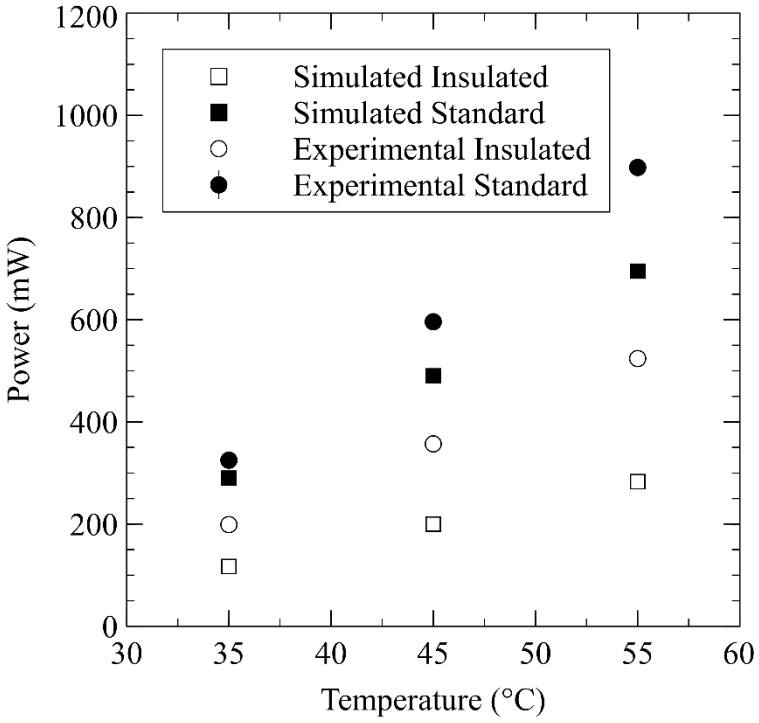

Figure 13: The power required in experiment (circles) and simulation (squares) to reach the three temperature setpoints (35 °C, 45 °C, and 55 °C) for the standard (solid) and insulated (hollow) chips. Comparing the experimental results to simulation the experimental standard chip required 12.1 %, 21.7 %, and 29.3 % more power to reach the three temperature setpoints while the experimental insulated chip required 69.5 %, 78.7 % and 85.5 % more power to reach the three temperature setpoints. While there is a discrepancy between simulation and experiment in both the standard and insulated chips the insulated chips discrepancy is much larger.

4.3 Improved Simulation Including the Thermocouple

Figure 14 shows the cross-sectional heat distribution when a thermocouple is added at the center of the chip to better match the experimental chips discussed in the previous section. The material dimensions and parameters used for these simulations can be found in Appendix A. The heat distribution changes significantly with the addition of the thermocouple by providing an easier path for heat to escape through the top of the chip. This is evident in the heat distribution of both chips but is particularly noticeable in the insulated chip where the thermocouple provides a way for the heat to bypass the insulation entirely leading to significantly higher temperatures at the top of the chip outside of the suspended bridge and considerably more heat energy lost to the environment. The k-type thermocouple (TP870, Extech, Boston, USA) was modeled as a 2 mm outer diameter silicone sheath around a 0.3 mm diameter cylinder of Chromel (90 % nickel, 10 % Chromium) and a 0.3 mm diameter cylinder of Alumel (95 % nickel, 2 % aluminum, 2 % manganese, 1 % silicon) [47]. The thermocouple was placed in a hole drilled 12 mm deep at the center of the top surface of each chip.

The addition of the thermocouple increases the power required to reach 35 °C, 45 °C, and 55 °C in both chips. In the standard chip the simulated required power increased from 0.290 W, 0.490 W, and 0.695 W without the thermocouple to 0.350 W, 0.594 W, and 0.838 W with the thermocouple. The thermocouple increased the power required to reach each of the temperature setpoints in the standard chip by 20.7 %, 21.2 %, and 20.6 % respectively. In the insulated chip the simulated required power increased from 0.117 W, 0.200 W, and 0.283 W without the thermocouple to 0.177 W, 0.301 W, and 0.428 W with the thermocouple. The thermocouple increased the required power to reach each of the temperature setpoints in the insulated chip by 51.30 %, 50.53 %, and 51.2 % respectively. The effect of the thermocouple was more significant in the insulated chip with an average increase in required power of 51.0 % compared the average increase in required power of 20.8 % in the standard chip. The thermocouple having a larger effect on the insulated design than it does on the standard design causes the energy savings from the added insulation to be only approximately 40 % compared to the approximately 60 % energy savings in the simulations without thermocouples. The reduction in energy

efficiency caused by the addition of the thermocouple makes them not an optimal method for temperature characterization or closing the loop on temperature control in heated microfluidic chips. Other methods such as thermochromic crystals and source measurement units would be more effective as they do not require a separate physical coupling approach and therefore would not affect the heat retention of the chip. These methods are discussed in more detail in Section 5.3 the future directions.

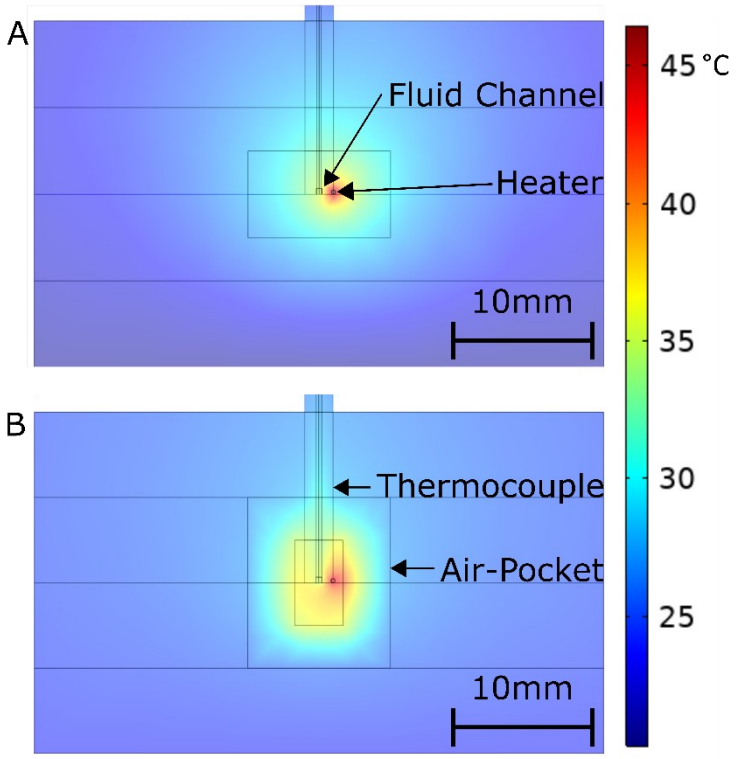

Figure 14: (A) Simulated cross-sectional heat distribution for the standard chip in 20 °C air. The temperature setpoint is 35 °C at the center of the fluid channel. The thermocouple is visible coming down from the top of the chip into the fluid channel. (B) Simulated cross-sectional heat distribution in the chip at steady-state conditions with insulating air pockets surrounding the fluid channel and heater. The thermocouple again comes down from the top of the chip and passes through the insulating air-pocket into the fluid channel at the center of the chip.

From the experimental values discussed in section 4.2 the required power values to reach steady state channel temperatures of 35 °C, 45 °C, and 55 °C were determined to be 0.325 W, 0.596 W, and 0.898 W for the standard chip and 0.199 W, 0.3578 W, and 0.524 W for

the insulated chip. The experimental values for the standard chip when compared to the values from the simulation with thermocouple are 7.15 % lower at 35 °C, 0.40 % higher at 45 °C, and 7.19 % higher at 55 °C. Similarly, the experimental values for the insulated chip are 12.2 % higher at 35 °C, 18.9 % higher at 45 °C and 22.7 % higher at 55 °C. The addition of the thermocouple mass reduced the average discrepancy between simulation and experiment from 21.0 to 0.1 % in the standard chip and 77.9 to 17.9 % in the insulated chip. Therefore, the addition of the thermocouple accounts for the majority of the noted difference. The remaining minor difference in the insulated chip is likely due to convection through the hole drilled for thermocouple access to the fluid channel. Table 2 summarizes the findings.

Table 4 Power requirements to reach the three temperature setpoints in the basic simulation, simulation with thermocouple, and experiment.

Temperature (°C)	Simulation (mW)		Simulation with Thermocouple (mW)		Experiment (mW)	
	Standard	Insulated	Standard	Insulated	Standard	Insulated
35	290	117	350	177	325	199
45	490	200	594	301	596	357
55	695	283	838	428	898	524

CHAPTER 5 BENCHTOP CHARACTERIZATION APPLIED TOWARD NITRATE

With the microfluidic chips built and found to have comparable temperature responses to those found in simulation, the microfluidic chips were ready to be applied to nitrate detection. First the method for preparing reagent is described, then the method for collecting and processing absorbance data. Next, the response time of the modified Griess assay needed to be characterized. To confirm and demonstrate the importance of temperature control this characterization was carried out at room temperature and also at an elevated temperature. After the temperature and reaction kinetics of the chemistry were characterized, the microfluidic chip with integral heater was ready to be tested as a functioning nitrate sensor in both the insulated and standard configuration.

5.1 Methods

5.1.1 Reagent Preparation

To prepare the modified Griess reagent, 2.5 g of vanadium (III) chloride, 1.25 g of sulfanilamide, 15 mL of concentrated HCl, and 0.125 g of NED (N-(1-aphthyl)ethylenediamine dihydrochloride) were dissolved in milli-Q water to reach a final volume of 500 mL. Chemicals and reagents used to make modified Griess reagent were sourced from Fisher Chemical (Waltham, MA, USA). The reagent was stored in a dark refrigerator at 4 °C to keep the reagent from degrading between uses [41]. When being used, the reagent bottle was wrapped in tinfoil to maintain the dark environment. Nightingale et al. found that the modified Griess reagent remains functional for at least 9 months stored at room temperature [5]. Nitrate standards were prepared from a 1000 µM stock made by diluting 14 mL of 100 ppm nitrogen as 442.68 ppm nitrate stock (NO3-N, R5457, RICCA Chemical Company, Arlington, TX, USA) to 100 mL using milli-Q water. The 1000 µM stock was then sequentially diluted to create the standards used in chip calibration. Eight concentrations of nitrate were applied to the thermally regulated optical cell for characterization. The concentrations used were 0.25 µM, 0.5 µM, 1 µM, 2

μM, 5 μM, 10 μM, 25 μM, and 50 μM, which were tested in ascending order, with each sample tested in triplicate to ensure repeatability.

5.1.2 Characterization Procedure

Two sets of standard and insulated chips were created: one set to measure temperature, and one set to validate chemistry. The temperature measurement chips were identical to the chemistry chips, except for an extra thermocouple port in the center of the chip for measuring channel temperature. The temperature chips were used to determine electrical current setpoints, as well as the time it would take to achieve the steady-state temperatures. Absorbance measurements were performed by automated fluid handling using two syringe pumps (Cavro XC, P/N 20 740 556-C, Tecan Systems, Männedorf, Switzerland). Absorbance measurements were performed using a green LED as the light source, centered at 527 nm with a FWHM of approximately 50 nm (C503B, Cree LED, Durham, NC, USA). The detector was a photodiode with a built-in 320 MΩ transimpedance gain amplifier (TSL257, AMS-TAOS Inc., Plano, TX, USA) that was used to acquire the light transmitted through the fluid path. One pump injected the sample and the other injected the reagent. The two syringe pumps delivered 1.5 mL of Griess reagent and 1.5 mL of sample or milli-Q water, each at a flow rate of 1.5 mL/min, into a mixing chip to create a blank sample. The mixing chip consisted of two input ports that merged into a 43 cm long serpentine channel with width and depth of 400 μm. The sample and reagent mixed while traveling through the channel then exited the mixing chip and entered the optical cell through a 58 cm long and 762 μm diameter fluoropolymer (FEP) tubing (IDEX 1520XL, Northbrook, IL, USA). The fluid must pass through 69 μL of dead volume in the chip and 265 μL of dead volume in the tubing giving a transit time of 7 s for the fluid to reach the optical cell after it began the mixing process. Multiple samples were introduced to the chip in an automated fashion using a selector valve (Vici Cheminert C65Z 10-port selector valve, Model No. C65-3710IA, Valco Instruments Co. Inc. Houston, TX, USA). While 3 mL of fluid are used for each measurement during these tests to ensure there would be no cross-talk between samples, only 69 μL of fluid is required to overcome the dead volume in the microfluidic chip. The automated switching between nitrate concentrations and milli-Q blanks was controlled with a custom script language developed in C. Electrical current was passed through a

300 µm diameter nichrome 80 wire using a CS1305 benchtop power source (Circuit Specialists, Tempe, AZ, USA) to heat the optical cell. A stopped flow approach was used, and the fluid was kept at the temperature setpoint for 10 min to allow the nitrate-to-nitrite reduction, as well as the Griess reaction to occur and the azo dye to form. Absorption measurements were continuously acquired from the fluid in the optical channel to determine the dye's concentration over time. The fluid was then pumped out of the chip into the waste container. The optical channel was then flushed with 15 mL of a 1 part milli-Q and 1 part Griess reagent mixture to clear the remaining sample and reduce crosstalk between samples.

5.1.3 Data Analysis

Absorbance of nitrate concentration was calculated using the Beer–Lambert law. The process was as follows. First, the LED was turned off, and the voltage output of the photodiode at the end of the absorbance cell was recorded over 15 s and averaged to obtain V_{Dark}. Second, the blank was introduced to the measurement channel by delivering 1 part milli-Q water and 1 part modified Griess reagent mixture, which was allowed to develop for 10 min. The voltage output over the last 15 s of the development time was averaged to obtain V_{Blank}. Third, the sample was introduced by injecting a mixture of 1 part known concentration of nitrate and 1 part modified Griess reagent to obtain V_{Sample}. V_{Dark} was subtracted from both V_{Sample} and V_{Blank} to negate the effect of light reaching the photodiode from sources not passing through the fluid channel.

$$V'_{Sample} = V_{Sample} - V_{Dark} \;\; || \;\; V'_{Blank} = V_{Blank} - V_{Dark} \tag{5.1}$$

The modified sample and blank voltages are denoted by V'_{Sample} and V'_{Blank}. Finally, the negative logarithm is taken of the modified sample voltage divided by the modified blank voltage to obtain the absorbance value of the known concentration of nitrate. The Beer–Lambert law holds that the absorbance of a medium (A) is equal to the concentration (c) of the absorbing species in that medium multiplied by the optical path length (l) multiplied by the molar attenuation coefficient of the species (ε). The molar attenuation coefficient is also a function of the wavelength (λ) of the light passing through the absorbing medium and, by extension, so is the absorbance. This equation

predicts a linear relationship between absorbance and nitrate concentration at the fixed peak wavelength of 527 nm.

$$A(\lambda) = \varepsilon(\lambda)cl = -log_{10}\left(\frac{V'_{Sample}}{V'_{Blank}}\right) \quad (5.2)$$

The optical cell was studied in previous work using a similar 25 mm path length inlaid absorbance cell [21]. The cell was simulated in OpticStudio 20.3.2 (Zemax, Kirkland, WA, USA) to determine the optical losses of the system, where the light enters the chip, passes through a blank sample in the fluid channel, and then leaves the chip. The LED light source reports a range of total light intensity from 16.8 cd to 90.5 cd. Using an average LED light intensity of 53.7 cd, the peak intensity was found to be 6.7 lumens/cm^2 (11 mW/cm^2) as the light entered the chip and 0.57 lumens/cm^2 (0.97 mW/cm^2) as the light exited the chip. For these calculations, a luminous efficiency of 588 lumens/W was used at the LED output peak wavelength of 527 nm. Zemax raytracing calculations, thus, indicate the optical losses of a 25.4 mm inlaid optical cell are more than 90 % of the incident light. The photodiode detector has a final irradiance responsivity of 1.56 V/(μW/cm^2) arising from the on-board transimpedance gain of 320 MΩ at the LED peak wavelength according to its datasheet. When the photodiode reports just below saturation (4.0-4.5 V), like during a blank, this equates to an optical intensity of 2.6–2.9 μW/cm^2. Even with 90 % optical loss from imperfections in the inlaid cell, the LED outputs 3 orders of magnitude higher light intensity than is required at the detector side (~1 mW/cm^2). Empirically, it was observed that misalignment of the LED and photodiode to the chip, as well as fabrication imperfections, lead to as much as 2 orders of magnitude of optical loss. Depending on alignment the LED is typically driven at 1–10 % of its maximum intensity, which was sufficient for reaching near saturation at the detector for nitrate measurement.

5.2 Calibration Using a Simple Cell

The experiment in this subsection was performed in collaboration with Edward Luy who also determined the parameters for the exponential fit used for extrapolation. Before

proceeding to perform the vanadium reduction assay with the on-chip heater, first the assay was characterized on a simpler chip without an integrated heater. Instead, an externally driven temperature source in the form of a custom enclosure around a hotplate was used. In other words, a stable temperature setpoints was established using an off-chip heater but the chemistry and optical measurement were performed in the inlaid microfluidic channel. Figure 15 shows the measured absorbance values at 527 nm over time, conducted in a simple inlaid optical absorbance cell in a thermally regulated chamber set at two temperatures. The nitrate colourimetric reaction was characterized by using a low (5 μM) and a high (50 μM) concentration of nitrate mixed in a 1:1 volumetric ratio with the modified Griess reagent at room temperature (22 °C) and heated conditions (47 °C). A setpoint of 47 °C was selected as the maximum temperature because it was observed that higher temperatures generated bubbles in the fluid that would interfere with the optical measurements unless sufficient degassing of fluids was performed. The formation of the coloured azo dye is a two-step chemical reaction, where nitrate is first reduced to nitrite by vanadium (III) chloride; then, the nitrite reacts with the Griess reagent to form the azo dye. The rate kinetics are largely dominated by the vanadium reduction reaction, as the Griess reaction is relatively quick, reaching 95% completion in under a minute at room temperature [21]. Therefore, the duration of colour development shown in Figure 15 is rate-limited primarily from the vanadium reduction in the two-step process.

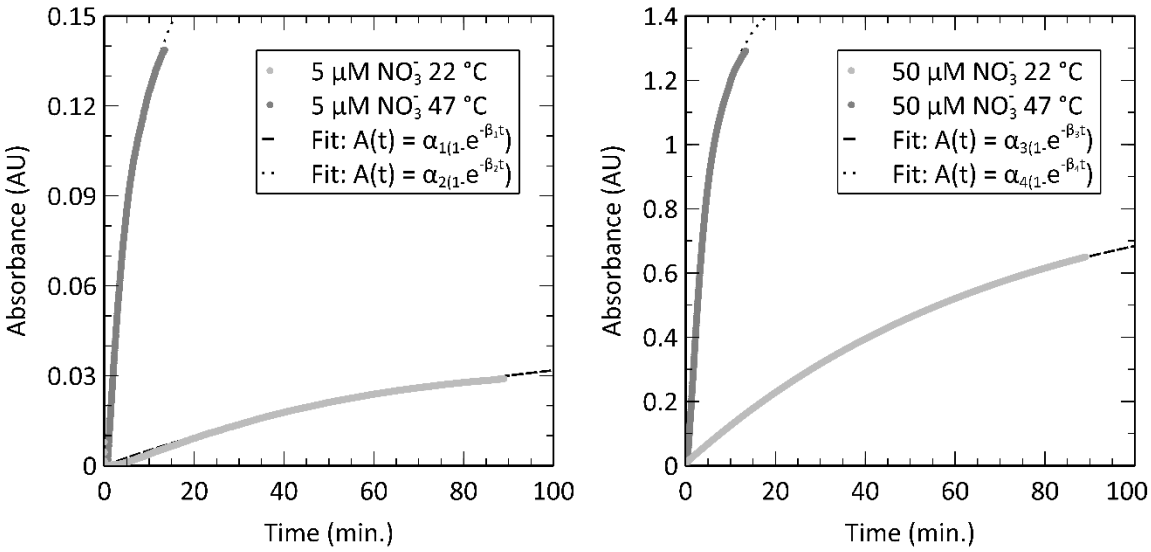

Figure 15: Reaction kinetics studied over 100 min for the vanadium reduction and Griess nitrate colour development assay described in the Materials and Methods. Absorbance measured at 527 nm versus time for a 5 µM nitrate concentration at 22 °C (RT) and at 47 °C, highlighting the slow colour development at low temperatures. The absorbance was 29 mAU after 90 min at 22 °C, whereas when heated to 47 °C, the same concentration resulted in an absorbance of 125 mAU after only 10 min. Fits to an exponential function are also shown, representing first-order reaction kinetics as described in text. Similar experimental study with a 50 µM nitrate concentration. High concentrations still benefit from heating, but not to the same degree as the lower concentrations.

The time to 95% completion was estimated using a single exponential fit, given that the time constant for the Griess reaction is significantly faster than the nitrate-to-nitrite reduction. For the 5 µM sample at 22 °C, $\alpha_1 = 0.0455$, $\beta_1 = 0.0002$, and for the 50 µM sample at 22 °C, $\alpha_2 = 0.1737$, $\beta_2 = 0.00211$. For the 5 µM sample at 47 °C, $\alpha_3 = 0.8835$, $\beta_3 = 0.000248$, and for the 50 µM sample at 47 °C, $\alpha_4 = 1.468$, $\beta_4 = 0.00283$. The extrapolation of this fit indicates that it would take 225 min to reach 95% completion at room temperature. Similarly, it would take 20 min to reach 95% completion at 47 °C. The reaction kinetics of the vanadium method for nitrate-to-nitrite reduction has been previously studied by Schnetger et al. at similar temperatures [27]. Schnetger evaluated the reaction kinetics at 23 °C and 45 °C, finding that the time required to reach 95% completion was 390 min and 31 min; or 92 % less time to achieve the same colour development when heated. This demonstrates similar improvements in reaction kinetics

as shown by the data in Figure 15 and the extrapolated time for 95% colour development, down from 225 min at 22 °C to 20 min at 47 °C, or 91.1% less time. Therefore, and as expected to save time and energy it will be imperative to heat the sample for as little time as possible, whilst ensuring sufficient time for colour development.

A colour development time of 10 min was arbitrarily selected for experiments, slightly higher than the reported literature values of 1-7 min to permit more data collection [6], [48]. While absorbance values are unitless, they have been labeled as AU or absorbance units for the sake of clarity. The data from Figure 15 show that the 22 °C experiments at 10 min resulted in absorbance values of 3.78 mAU for the 5 μM sample and 125 mAU for the 50 μM sample. Therefore, a 10 min development time without heating yielded insufficient colour development for most oceanographic or in situ sensing purposes, as the setup typically is characterized by a noise floor of ±1 mAU, or a lower limit of 1–2 μM without heating. However, at 47 °C and 10 min, the absorbances from Figure 15 were 125 mAU for the 5 μM sample and 1.20 AU for the 50 μM sample. The increased colour development indicates that a nanomolar limit of detection is possible with heating.

5.3 Nitrate Detection Using Inlaid Optical Cell with Integral Heater

The chips with integrated heaters described in the previous chapters were then utilized to perform a calibration using eight nitrate standards with concentrations from 0.25 μM to 50 μM. Figure 16 shows the raw voltage data gathered from the photodiodes from both the standard and insulated chips for all eight standards run in triplicate. The procedure for this test is described in brief here and in detail in Section 5.1. Light was directed through a 25 mm-long microfluidic channel and detected by a photodiode on the other end of the channel. The samples form azo dye in proportion to the concentration of nitrate, thereby reducing the amount of light that reaches the photodiode and decreasing its voltage output. Figure 16A shows the entire data sequence collected on the standard chip, of eight concentrations measured in triplicate, totaling 24 sample measurements and 24 blank

measurements. Figure 16B shows a plot of the same data from Figure 16A, but zoomed in on the triplicate of the 5 μM samples. The second 5 μM sample in Figure 16B labels the blank measurement and the sample measurement. The plateaus in Figure 16B represent the blank (10 min per), the decaying voltage represents the sample colour development (10 min per), and the stochastic data between plateaus and decays represent the time where pumping (4 min per) is occurring. During the pumping phase, a bi-modal data trend is noted; when the fluid is stopped, the voltage reading is approximately that of a blank and when fluid is being pumped, the voltage is approximately 0.4 V higher due to Schlieren effect arising from a parabolic pressure-driven flow profile. The withdraw and inject sequence of the syringe pumping also introduces a small amount of noise about these two-levels (fluid stopped and fluid pumping). Similarly, Figure 16C shows the entire data sequence collected on the insulated chip, of eight concentrations measured in triplicate, totaling 24 sample measurements and 24 blank measurements. Figure 16D shows a plot of the same data from Figure 16C, but zoomed in on the triplicate of the 5 μM samples. The same trends are noted for pumping, blanks, and samples.

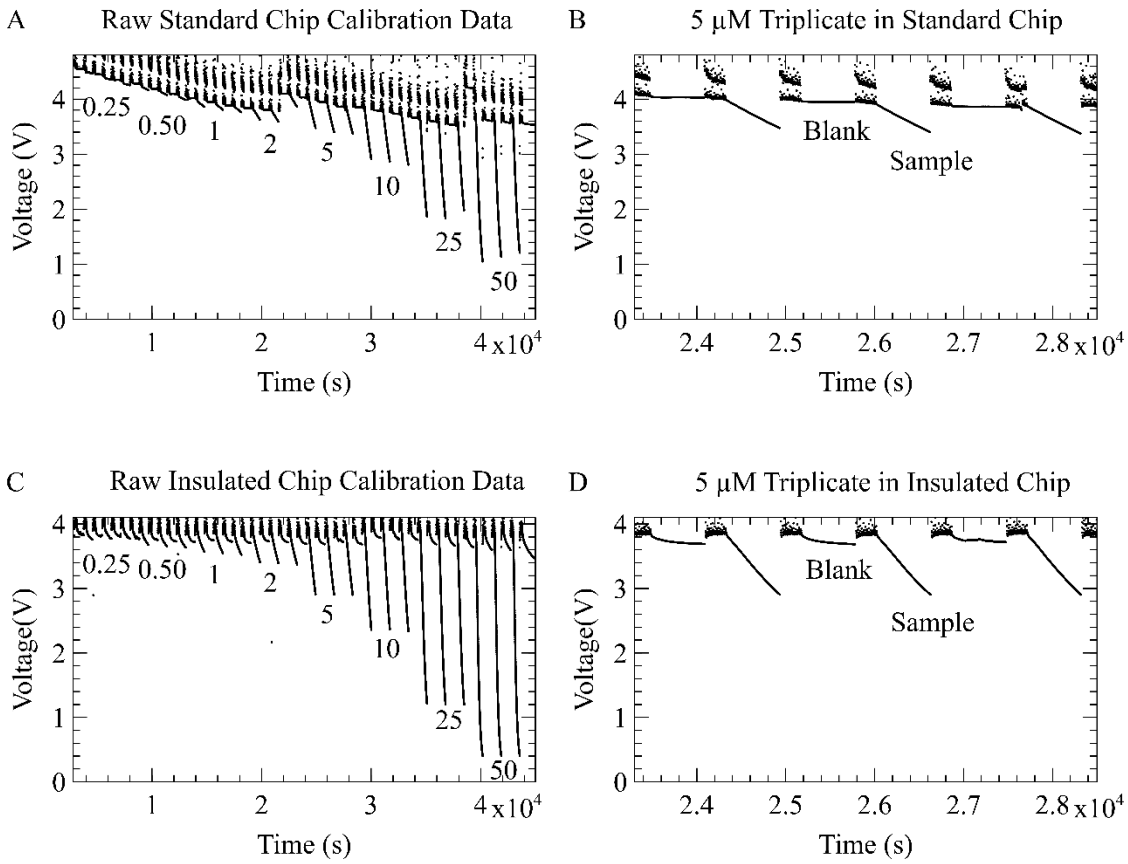

Figure 16: Raw photodiode voltage output over time collected during the calibration procedure. (A) The voltage output from the standard chip calibration. Each of the 8 sample concentrations were tested three times with blank measurements taken between each sample. As expected, higher concentrations cause larger drops in voltage. A downward drift is visible in the data and is discussed in the text. (B) A zoomed in view of the standard chip raw voltage data showing only the 5 µM triplicate. The second 5 µM sample and its associated blank measurement are labeled. Preceding each blank and each sample is a period of noise caused by fluid moving through the optical channel during the pumping process. (C) Voltage output from the insulated chip calibration. The downward drift visible in the standard chip calibration was not present; however, there was some crosstalk between samples. (D) Zoomed in view of the insulated chip data for the 5 µM triplicate.

The voltage of the blanks in the standard chip gradually dropped over the course of the 700 min experiment in Figure 16A, from a starting value of 4.6 V down to a final value of 3.5 V. This 1.1 V downward drift was likely caused by a bubble nucleating in the channel. This hypothesis is supported by the rapid jump in the blanks after the second 2

µM measurement; the blank rises instantaneously from 3.8 V to 4.1 V. Again, a jump in the blank preceding the first 50 µM sample, where signal jumped from 3.5 V to 4.2 V then fell back to 3.6 V for the next blank. Microfluidic devices are prone to small bubbles entering the chip during pumping and obscuring optical measurements [49]. However, the downward drift in Figure 16A did not affect the absorbance calculations, as blank measurements were acquired before every sample measurement. The insulated chip had a negligible downward drift in blank values, shown in Figure 16C, starting at 3.8 V and falling to 3.6 V over the 700 min. A small degree of crosstalk between samples is observable in Figure 16C, where the blank measurements show colour development toward the higher concentrations.

To evaluate the expected linear relationship as per the Beer–Lambert law, the raw data from Figure 16A and C were used to calculate the absorbance values versus concentrations. Figure 17 shows the measured absorbance values for each sample plotted against their concentrations. The standard chip data are shown as solid black circles, while the insulated chip data are shown as black outlines around white circles. Figure 17A shows the entire range of concentrations tested and Figure 17B plots the first five concentrations from 0.25 µM to 5 µM. Each data point in Figure 17 is an average of the three consecutive absorbance measurements. Standard deviations are calculated and included for each point; however, they are often not visible, as values are typically below 10 mAU in Figure 17A and below 2 mAU in Figure 17B. The TSL257 photodiode's datasheet reports a measurement error of 200 µVrms. With the 5V blank voltage here, this would lead to a 10^{-5} AU error, making the optical error negligible compared to the triplicate standard deviation. A linear fit for each dataset is also shown in Figure 17A,B. The line of best fit was found to be $A(x) = 0.0108x$ for the standard chip and $A(x) = 0.0198x$ for the insulated chip, where x is the nitrate concentration in µM and A(x) is the Absorbance value in AU at a given nitrate concentration. Both lines were held to a y-intercept of 0 during fitting in accordance with the Beer–Lambert law outlined in Equation (3.2). The fits had R-squared values of better than 0.99, and a root mean square error (RMSE) of 8.4 mAU for the standard chip and 3.1 mAU for the insulated chip. These metrics confirm the expected linear relationship.

From the Beer–Lambert law, the slope of the absorbance versus concentration relationship is the product of the length of the optical interrogation channel (25 mm) and the molar attenuation coefficient of the species at a fixed wavelength. The slopes of the standard and insulated chip's calibration data result in molar attenuation coefficients of 0.00432 $(\mu M\ cm)^{-1}$ and 0.00792 $(\mu M\ cm)^{-1}$, respectively. The coefficients from these experiments are lower than the reported value of 0.0269 $(\mu M\ cm)^{-1}$ by Luy et al. [21]. The main contributor to the underreported molar attenuation coefficients is the incomplete colour development. Here, measurements were taken after 10 min and not given time to react fully, whereas in Luy et al., the samples were premixed and left for several hours. The difference between the two attenuation coefficients (i.e., the slopes of Figure 17) is also attributed to varying degrees of colour development completion. The reactions reached different levels of completion in the standard and insulated chips. Both chips were driven with the currents that were determined to achieve a channel temperature of 35 °C in Figure 12; however, those current setpoints were determined in chips with integrated thermocouples, while the calibration curves were performed in chips without thermocouples. The thermocouple increased the thermal mass as outlined above and described in Chapter 4.3. The removal of the thermocouple in the chips used to gather the data in Figures 16 and 17 leads to the chips' calibration curves being performed at different temperatures. Based on COMSOL simulations the insulated chip calibration curve was performed at an estimated 43 °C, while the standard chip calibration curve was performed at an estimated 38 °C. The higher temperature in the insulated chip caused the nitrate-to-nitrite reduction to occur more quickly and, as a result, increased the absorbance reading for each concentration. At both temperatures, the linear relationship is preserved, indicating successful acceleration of the reaction kinetics in an on-chip optical cell using an integral heater.

The limit-of-detection (LOD) was determined using the triple-sigma literature method, which uses three times the standard deviation observed during blank measurements [21], [48], [50]. From these standard deviations, the LOD of the system was determined to be 5 nM for the standard chip and 20 nM for the insulated chip. The average standard deviation of each blank was 0.196 mAU for the standard chip and 1.170 mAU for the insulated chip. Ultimately, a novel microfluidic architecture for performing

thermally regulated optical absorbance measurements on-chip was demonstrated that achieves nanomolar LODs and improves energy efficiency by at least 40% using integral air pockets.

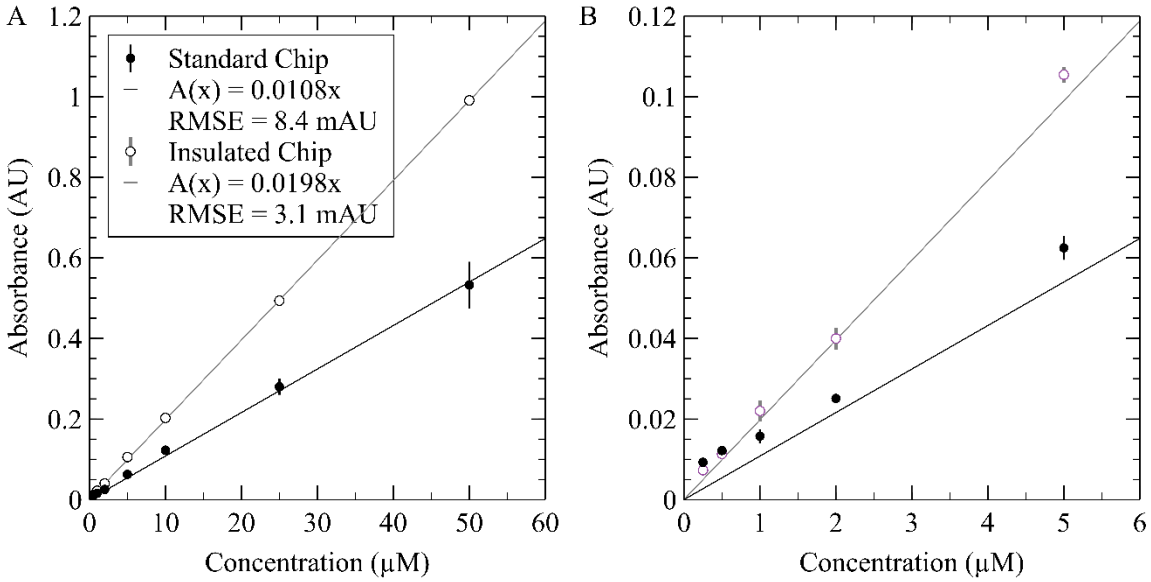

Figure 17: Processed calibration data demonstrating a linear relationship between absorbance and concentration in both the standard and insulated chips. Standard chip was tested at 38 °C while the insulated chip was held at 43 °C. (A) Full calibration curve showing concentrations ranging from 0.25 μM to 50 μM. (B) Zoomed in calibration curve showing concentrations from 0.25 μM to 5 μM, which can be hard to visualize on the full-scale calibration curve.

With the chips having been simulated, their temperature and photometric outputs having been characterized, and their function as nitrate sensors validated, the next step is to deploy the chips on a sensor stack that can be deployed *in situ*. Prior to the chips with integral heaters being deployed, simpler chips designed to detect nitrite were deployed as discussed in the next chapter.

With the successful benchtop tests as well as the successful deployment of the nitrite sensor, it is clear that this method for *in situ* reagent based measurements is effective. If the sensor described in this chapter were to be combined with the thermally regulated optical cell described in previous chapters an *in situ* nitrate sensor using gold standard colourimetric methods could be realized while mitigating the increase in power draw generated by the addition of the heater.

CHAPTER 6 CONCLUSION AND FUTURE DIRECTIONS

6.1 Summary

This thesis demonstrates a method for integrating heaters into inlaid microfluidic optical cells and reducing the power draw of that integral heater. This reduction in power draw was achieved by insulating the heated areas of the cell from the rest of the microfluidic chip, and the environment as a whole. An *in situ* nutrient sensor for the detection of nitrite was designed such that the thermally regulated microfluidic chip could be integrated onto it to allow for nitrate detection. A chip with and a chip without these insulating air pockets were simulated to allow rapid optimization of the design and to characterize their heat response . Once the insulated chip was found, in simulation, to reduce the power draw from heating by an average of 49.3 % the chips were constructed physically. These chips' temperature responses were characterized, and their outputs were found to be in reasonable agreement with those found in simulation with the power requirements being reduced by an average of 40.2 %. The chips were then characterized as nitrate sensors and found to be capable of detecting nanomolar concentrations of nitrate with strong linearity and a limit of detection of 20 nM.

6.2 Future Directions

6.2.1 Closed Loop Temperature Control

Future work will see a closed-loop implementation of the thermal/heater design and associated analysis. The heater described in this thesis utilizes open-loop direct current temperature control; however, with a closed-loop heater design the system could be improved significantly. This would be vital to monitoring nitrate levels in waterways where the chip will be submerged, and the boundary condition will be an unknown temperature. A closed-loop temperature control design would allow the channel temperature to be kept consistent even with the ambient temperature changing around it, thereby allowing for consistent reaction times. The addition of a proportional–integral–derivative (PID) temperature controller would allow the channel to be brought to and held

at a setpoint temperature faster. The system could be run in an overdamped mode to reach elevated temperatures quickly; however, temperature overshoot would need to be minimized to avoid approaching the glass transition temperature of PMMA, as well as to avoid bubble generation in the fluid sample that could affect the optical measurements. PID control was not implemented in this design because it was not necessary for the benchtop proof of concept described in this thesis; however, it will be needed when the design is applied to *in situ* testing. Even when a PID is implemented for *in situ* deployment, the reaction kinetics for nitrate-to-nitrite reduction will impose a lower limit of several minutes of active heating time. Regardless, the thermal insulation provided by the air pocket design will enable steady state to be attained faster with or without a PID compared to non-insulated designs.

6.2.2 Improved temperature sensing

Optically monitoring thermochromic crystals embedded in the channel is a promising alternative to the thermocouple for closing the loop. Thermochromic crystal solutions change their colour based on the fluid temperature and would allow the temperature to be monitored optically, removing the need for physical coupling between the heated and non-heated areas of the microfluidic chip [51]. Other methods of wireless temperature reading are also available. Subthreshold ring oscillators have been demonstrated as a means of generating a signal with a temperature-dependent frequency that could be transmitted wirelessly through the air pocket [52]. A source-measurement-unit (SMU) could also be implemented using the relationship between the wire temperature and its resistivity, as demonstrated for platinum [53]. Using the SMU method, the temperature at the heater can be monitored by reading its resistance and allows for a much simpler temperature sensor than the wireless alternatives without requiring any additional physical connection between the suspended optical cell and the rest of the chip. Of these methods, the SMU approach is the most amenable to integration with the suspended optical heater design, given that the same heating wire can be used as the sensing element.

6.2.3 Integrated Nitrate Sensor Stack

The insulated nitrate chip design will be integrated with a sensor stack similar to the one described in chapter 2 to allow the nitrate sensor to be tested *in situ*. This will be important as the purpose of the insulation is to reduce the power draw from the sensor thereby allowing it to remain in place longer without requiring new or larger batteries. The design outlined in chapters 2 and 5 will need to be altered to allow for power to be coupled through the can into the microfluidic chip. In the event that this proves difficult to do by directly passing wires from the rest of the sensor to the chip, this could be done through induction, using coupled coils to pass power from the can to the chip without requiring the seal to be broken and risking having more places water might enter and harm the sensor.

6.2.4 Field Testing

Once the nitrate sensor stack is complete it will need to be tested *in situ*. This will be accomplished by placing it in an environment similar to the one discussed in chapter 2. Ideally somewhere accessible with low traffic and where nitrate levels will change appreciably and predictably over the course of a day. Ideally, onboard blank and standard concentrations would be included in the sensor like those included in the sensor outlined by Morgan et al. [24]. Additionally, samples will need to be collected from the environment at several points during the *in situ* tests and evaluated using an existing nitrate analyser to provide a baseline that the effectiveness of the sensor can be compared against. If this is to be done before fully integrating the heater it could be placed in an environment with very high nitrate concentrations such as a river that passes by farmland that may allow nitrate runoff to contaminate the river in concentrations high enough to be detected quickly without heating.

6.3 Other Power Saving Options

Figure 18 outlines the power budget of four different senser configurations. Each system's power budget is split into 5 modules: control, heating, optics, motor driver, and motor, and displayed as a pie chart. Measurements are assumed to require 1 min of

pumping and 10 min of sample development for each measurement. In the first system the senser is controlled by a Raspberry Pi Zero W and uses an uninsulated chip. This would be the power usage of the sensor described in chapter 2 if it were heated to detect nitrate. In this system energy is primarily being used for control, motor, and heating with those modules using 35 %, 34 %, and 21 % of the total power respectively. When on chip insulation is integrated into that design for design 2 the percentage of the power used for heating drops to 14 % leaving the control and motor as the most significant power draws at 38 %, and 37 % respectively.

The control method is the simplest place to reduce power consumption. The Raspberry Pi Zero W was chosen for the prototype because they are simple to operate, easily replaceable, and able to handle sensor control, datalogging, and Wi-Fi connection in the same chip. However, the Raspberry Pi Zero W requires a lot of power when compared to a dedicated microcontrollers like the PIC24FJ128GC010 (Microchip Technology, Chandler, AZ, USA) and STM32F7 (STMicroelectronics, Plan-les-Ouates, Switzerland) used in the nutrient sensor described by Morgan et al. [24]. In design 3, with the low power control method, the power used by the controllers drops to 6 % of the total power leaving the motor and heating as the largest power draws at 49 % and 30 % respectively. With low power control methods and insulated heating, the motor becomes the highest power draw by far at 56 % with heating next at only 21 %.

As for total power used, the bar graph on the right of figure 18 shows the total energy used per sample for each sensor design. Design 1 is the least optimised requiring 1030 J per sample. For design 2, optimising heating reduces the power draw to 950 J, while for design 3, optimising control methods reduces the power draw to 720 J. When both heating and control are optimised in design 4 the power draw reduces to 630 J, about 61 % of the power that would be used by design 1. This design would consume a comparable amount of energy to cutting edge sensors like the one outlined by Mowlem et al. which consumed approximately 500 J per measurement without heating and using a much shorter measurement time [54].

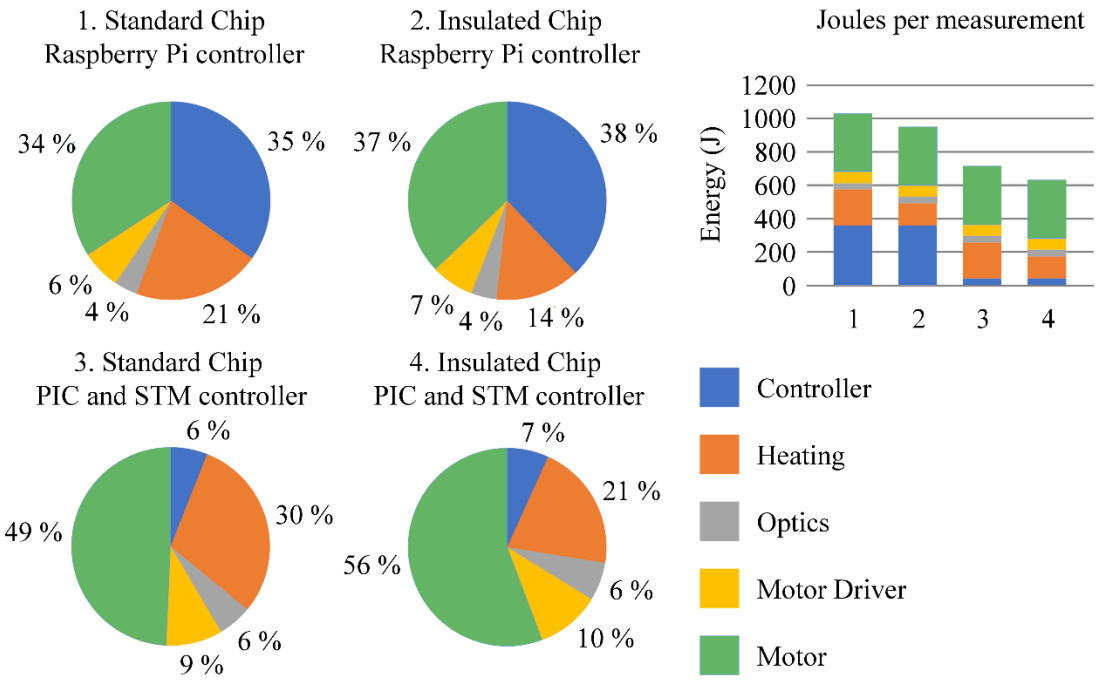

Figure 18: Power budgets for four different configurations of the nutrient sensor. (Left) Pie charts outlining the percentage of total power used by five different modules in four senser designs. Power budgets with and without insulation are compared as well as two different control methods. (Top Right) Total energy per measurement for the four sensor configurations is shown with a bar graph. The bars are colour coded to show the contribution of each module to the total power. Module power is calculated assuming 1 min of pumping and 10 min of data collection per sample. (Bottom Left) The colour code for the pie charts and bar graph is displayed.

BIBLIOGRAPHY

[1] A. Tovar, C. Moreno, M. P. Mánuel-Vez, and M. García-Vargas, "A simple automated method for the speciation of dissolved inorganic nitrogen in seawater," *Anal. Chim. Acta*, vol. 469, no. 2, Art. no. 2, Oct. 2002, doi: 10.1016/S0003-2670(02)00752-3.

[2] D. Justic, R. E. Turner, and N. N. Rabalais, "Climatic influences on riverine nitrate flux: Implications for coastal marine eutrophication and hypoxia," *Estuaries*, vol. 26, no. 1, Art. no. 1, Feb. 2003, doi: 10.1007/BF02691688.

[3] M. L. S. Diego-McGlone, R. V. Azanza, C. L. Villanoy, and G. S. Jacinto, "Eutrophic waters, algal bloom and fish kill in fish farming areas in Bolinao, Pangasinan, Philippines," *Mar. Pollut. Bull.*, vol. 57, no. 6, Art. no. 6, 2008, doi: https://doi.org/10.1016/j.marpolbul.2008.03.028.

[4] H. Galalgorchev, "Who Guidelines for Drinking-Water Quality," in *Iwsa Specialized Conference on Quality Aspects of Water Supply*, F. Fiessinger, Ed., Oxford: Blackwell Scientific Publ, 1992, pp. 1–16.

[5] A. M. Nightingale *et al.*, "A Droplet Microfluidic-Based Sensor for Simultaneous in Situ Monitoring of Nitrate and Nitrite in Natural Waters," *Environmental Science & Technology*, vol. 53, no. 16. Amer Chemical Soc, 1155 16TH ST, NW, Washington, DC 20036 USA, pp. 9677–9685, Aug. 20, 2019. doi: 10.1021/acs.est.9b01032.

[6] A. D. Beaton *et al.*, "An automated microfluidic colourimetric sensor applied in situ to determine nitrite concentration," *Sens. Actuators B-Chem.*, vol. 156, no. 2, Art. no. 2, Aug. 2011, doi: 10.1016/j.snb.2011.02.042.

[7] G. MacIntyre *et al.*, "ISUS/SUNA Nitrate Measurements in Networked Ocean Observing Systems," in *Oceans 2009, Vols 1-3*, New York: Ieee, 2009, pp. 2125-+.

[8] A. D. Beaton *et al.*, "Lab-on-Chip Measurement of Nitrate and Nitrite for In Situ Analysis of Natural Waters," *Environ. Sci. Technol.*, vol. 46, no. 17, Art. no. 17, Sep. 2012, doi: 10.1021/es300419u.

[9] M. McCaul *et al.*, "Nutrient Analysis in Arctic Waters Using a Portable Sensing Platform.," 2021, doi: 10.3389/fsens.2021.711592.

[10] T. Yin *et al.*, “A Novel Lab-on-Chip Spectrophotometric pH Sensor for Autonomous In Situ Seawater Measurements to 6000 m Depth on Stationary and Moving Observing Platforms,” *Environ. Sci. Technol.*, vol. 55, no. 21, pp. 14968–14978, Nov. 2021, doi: 10.1021/acs.est.1c03517.

[11] A. M. Nightingale, A. D. Beaton, and M. C. Mowlem, “Trends in microfluidic systems for in situ chemical analysis of natural waters,” *Sens. Actuators B-Chem.*, vol. 221, pp. 1398–1405, Dec. 2015, doi: 10.1016/j.snb.2015.07.091.

[12] T. Fukuba and T. Fujii, “Lab-on-a-chip technology for in situ combined observations in oceanography,” *Lab. Chip*, vol. 21, no. 1, pp. 55–74, Jan. 2021, doi: 10.1039/D0LC00871K.

[13] A. C. Edwards, P. S. Hooda, and Y. Cook, “Determination of nitrate in water containing dissolved organic carbon by ultraviolet spectroscopy,” *Int. J. Environ. Anal. Chem.*, vol. 80, no. 1, Art. no. 1, 2001, doi: 10.1080/03067310108044385.

[14] “Optical Absorption Characteristics, Spatial Distribution, and Source Analysis of Colored Dissolved Organic Matter in Wetland Water around Poyang Lake,” *Water*, vol. 13, no. 3, Art. no. 3, 2021, doi: http://dx.doi.org.ezproxy.library.dal.ca/10.3390/w13030274.

[15] M. A. P. Mahmud *et al.*, “Recent progress in sensing nitrate, nitrite, phosphate, and ammonium in aquatic environment,” *Chemosphere*, vol. 259, p. 127492, Nov. 2020, doi: 10.1016/j.chemosphere.2020.127492.

[16] S. S. M. Hassan, A. Galal Eldin, A. E.-G. E. Amr, M. A. Al-Omar, A. H. Kamel, and N. M. Khalifa, “Improved Solid-Contact Nitrate Ion Selective Electrodes Based on Multi-Walled Carbon Nanotubes (MWCNTs) as an Ion-to-Electron Transducer,” *Sensors*, vol. 19, no. 18, Art. no. 18, Jan. 2019, doi: 10.3390/s19183891.

[17] Johann Peter Griess, “Preliminary notice of the reaction of nitrous acid with picramic acid and aminonitrophenol,” *Ann Chem Pharm*, vol. 106, pp. 123–125, 1858.

[18] Z. Yilong, Z. Dean, and D. li, “Electrochemical and Other Methods for Detection and Determination of Dissolved Nitrite: A Review,” *Int. J. Electrochem. Sci.*, vol. 10, pp. 1144–1168, Feb. 2015.

[19] K. S. Johnson and R. L. Petty, “Determination of Nitrate and Nitrite in Seawater by Flow Injection Analysis,” *Limnol. Oceanogr.*, vol. 28, no. 6, Art. no. 6, 1983.

[20] S. Wang, K. Lin, N. Chen, D. Yuan, and J. Ma, “Automated determination of nitrate plus nitrite in aqueous samples with flow injection analysis using vanadium (III) chloride as reductant,” *Talanta*, vol. 146, pp. 744–748, 2016, doi: https://doi.org/10.1016/j.talanta.2015.06.031.

[21] E. A. Luy, S. C. Morgan, J. J. Creelman, B. J. Murphy, and V. J. Sieben, “Inlaid microfluidic optics: absorbance cells in clear devices applied to nitrite and phosphate detection,” *J. Micromechanics Microengineering*, vol. 30, no. 9, Art. no. 9, Sep. 2020, doi: 10.1088/1361-6439/ab9202.

[22] P. Petsul, G. Greenway, and S. Haswell, “The development of an on-chip micro-flow injection analysis of nitrate with a cadmium reductor,” *Analytica Chimica Acta*, vol. 428, no. 2. Elsevier Science BV, PO BOX 211, 1000 AE Amsterdam, Netherlands, pp. 155–161, Feb. 09, 2001. doi: 10.1016/S0003-2670(00)01244-7.

[23] S. C. Morgan, A. D. Hendricks, M. L. Seto, and V. J. Sieben, “A Magnetically Tunable Check Valve Applied to a Lab-on-Chip Nitrite Sensor,” *Sensors*, vol. 19, no. 21, p. 4619, Nov. 2019, doi: 10.3390/s19214619.

[24] S. Morgan, E. Luy, A. Furlong, and V. Sieben, “A submersible phosphate analyzer for marine environments based on inlaid microfluidics,” *Anal. Methods*, vol. 14, no. 1, pp. 22–33, Dec. 2021, doi: 10.1039/D1AY01876K.

[25] Q.-H. Wang *et al.*, “Methods for the detection and determination of nitrite and nitrate: A review,” *Talanta*, vol. 165, pp. 709–720, Apr. 2017, doi: 10.1016/j.talanta.2016.12.044.

[26] M. Yaqoob, B. F. Biot, A. Nabi, and P. J. Worsfold, “Determination of nitrate and nitrite in freshwaters using flow-injection with luminol chemiluminescence detection,” *Luminescence*, vol. 27, no. 5, Art. no. 5, 2012, doi: https://doi.org/10.1002/bio.1366.

[27] B. Schnetger and C. Lehners, “Determination of nitrate plus nitrite in small volume marine water samples using vanadium(III)chloride as a reduction agent,” *Mar. Chem.*, vol. 160, pp. 91–98, Mar. 2014, doi: 10.1016/j.marchem.2014.01.010.

[28] J. Sun, X. Zhang, M. Broderick, and H. Fein, “Measurement of Nitric Oxide Production in Biological Systems by Using Griess Reaction Assay,” *Sensors*, vol. 3, no. 8, Art. no. 8, Aug. 2003, doi: 10.3390/s30800276.

[29] S. L. Kharatyan, H. A. Chatilyan, A. S. Mukasyan, D. A. Simonetti, and A. Varma, “Effect of heating rate on kinetics of high-temperature reactions: Mo-Si system,” *AIChE J.*, vol. 51, no. 1, pp. 261–270, 2005, doi: 10.1002/aic.10303.

[30] S. Damilos, A. N. P. Radhakrishnan, G. Dimitrakis, J. Tang, and A. Gavriilidis, “Experimental and computational investigation of heat transfer in a microwave-assisted flow system,” *Chem. Eng. Process. - Process Intensif.*, vol. 142, p. 107537, Aug. 2019, doi: 10.1016/j.cep.2019.107537.

[31] D. Issadore, K. J. Humphry, K. A. Brown, L. Sandberg, D. A. Weitz, and R. M. Westervelt, "Microwave dielectric heating of drops in microfluidic devices," *Lab on a Chip*, vol. 9, no. 12. Royal Soc Chemistry, Thomas Graham House, Science Park, Milton RD, Cambridge CB4 0WF, Cambs, England, pp. 1701–1706, 2009. doi: 10.1039/b822357b.

[32] T.-Y. Chen, M. Baker-Fales, and D. G. Vlachos, "Operation and Optimization of Microwave-Heated Continuous-Flow Microfluidics," *Ind. Eng. Chem. Res.*, vol. 59, no. 22, Art. no. 22, Jun. 2020, doi: 10.1021/acs.iecr.0c01650.

[33] V. Miralles, A. Huerre, F. Malloggi, and M.-C. Jullien, "A Review of Heating and Temperature Control in Microfluidic Systems: Techniques and Applications," *Diagnostics*, vol. 3, no. 1, Art. no. 1, Jan. 2013, doi: 10.3390/diagnostics3010033.

[34] R. M. Guijt, A. Dodge, G. W. K. van Dedem, N. F. de Rooij, and E. Verpoorte, "Chemical and physical processes for integrated temperature control in microfluidic devices," *Lab. Chip*, vol. 3, no. 1, Art. no. 1, 2003, doi: 10.1039/b210629a.

[35] R. G. Spruit, J. T. van Omme, M. K. Ghatkesar, and H. H. P. Garza, "A Review on Development and Optimization of Microheaters for High-Temperature In Situ Studies," *J. Microelectromechanical Syst.*, vol. 26, no. 6, Art. no. 6, Dec. 2017, doi: 10.1109/JMEMS.2017.2757402.

[36] V. Hoang N., "Thermal Management Strategies for Microfluidic Devices," Masters Thesis, University of Alberta, Edminton Alberta Canada, 2008.

[37] Y. Zhao *et al.*, "Heavily-Doped Bulk Silicon Sidewall Electrodes Embedded between Free-Hanging Microfluidic Channels by Modified Surface Channel Technology," *Micromachines*, vol. 11, no. 6, Art. no. 6, Jun. 2020, doi: 10.3390/mi11060561.

[38] M. Dijkstra, M. J. de Boer, J. W. Berenschot, T. S. J. Lammerink, R. J. Wiegerink, and M. Elwenspoek, "Miniaturized thermal flow sensor with planar-integrated sensor structures on semicircular surface channels," *Sens. Actuators Phys.*, vol. 143, no. 1, Art. no. 1, May 2008, doi: 10.1016/j.sna.2007.12.005.

[39] T. V. P. Schut, R. J. Wiegerink, and J. C. Lotters, "mu-Coriolis Mass Flow Sensor With Differential Capacitive Readout," *Ieee Sens. J.*, vol. 21, no. 5, Art. no. 5, Mar. 2021, doi: 10.1109/JSEN.2020.3042078.

[40] J. Martinez-Quijada *et al.*, "Deterministic Design of Thin-Film Heaters for Precise Spatial Temperature Control in Lab-on-Chip Systems," *J. Microelectromechanical Syst.*, vol. 25, no. 3, Art. no. 3, Jun. 2016, doi: 10.1109/JMEMS.2016.2536561.

[41] E. Garcia-Robledo, A. Corzo, and S. Papaspyrou, “A fast and direct spectrophotometric method for the sequential determination of nitrate and nitrite at low concentrations in small volumes,” *Marine Chemistry*, vol. 162. Elsevier, Radarweg 29, 1043 NX Amsterdam, Netherlands, pp. 30–36, May 20, 2014. doi: 10.1016/j.marchem.2014.03.002.

[42] “Transport Phenomena, Revised 2nd Edition | Wiley,” *Wiley.com*. https://www.wiley.com/en-gb/Transport+Phenomena%2C+Revised+2nd+Edition-p-9780470115398 (accessed Jan. 28, 2022).

[43] U. Ali, K. J. B. A. Karim, and N. A. Buang, “A Review of the Properties and Applications of Poly (Methyl Methacrylate) (PMMA),” *Polym. Rev.*, vol. 55, no. 4, Art. no. 4, Oct. 2015, doi: 10.1080/15583724.2015.1031377.

[44] H. Bruus, *Theoretical Microfluidics*, First. in Oxford Master Series in Condensed Matter Physics. Oxford: Oxford University Press, 2008.

[45] Y. Touloukian, R. Powel, C. Ho, and P. Klemens, *Thermophysical Properties of Matter*, vol. Volume 3. in The TPRC Data Series, vol. Volume 3. Defense Technical Information Center, 1970.

[46] A. Curran, M. Klein, M. Hepokoski, and C. Packard, “Improving the accuracy of infrared measurements of skin temperature,” *Extreme Physiol. Med.*, vol. 4, no. Suppl 1, Art. no. Suppl 1, Sep. 2015, doi: 10.1186/2046-7648-4-S1-A140.

[47] R. Lima de Oblitas, F. de Sá Teixeira, and M. C. Salvadori, “Determination of the composition and thickness of chromel and alumel thin films on different substrates by quantitative energy dispersive spectroscopy analysis,” *Microsc. Res. Tech.*, vol. 85, no. 2, pp. 437–446, 2022, doi: 10.1002/jemt.23917.

[48] V. J. Sieben, C. F. A. Floquet, I. R. G. Ogilvie, M. C. Mowlem, and H. Morgan, “Microfluidic colourimetric chemical analysis system: Application to nitrite detection,” *Anal. Methods*, vol. 2, no. 5, Art. no. 5, May 2010, doi: 10.1039/C002672G.

[49] X. He, B. Wang, J. Meng, S. Zhang, and S. Wang, “How to Prevent Bubbles in Microfluidic Channels,” *Langmuir*, vol. 37, no. 6, Art. no. 6, Feb. 2021, doi: 10.1021/acs.langmuir.0c03514.

[50] A. Shrivastava, “Methods for the determination of limit of detection and limit of quantitation of the analytical methods,” *Chron. Young Sci.*, vol. 2, pp. 21–25, Jun. 2011, doi: 10.4103/2229-5186.79345.

[51] V. N. Hoang, G. V. Kaigala, and C. J. Backhouse, “Dynamic temperature measurement in microfluidic devices using thermochromic liquid crystals,” *Lab. Chip*, vol. 8, no. 3, Art. no. 3, Feb. 2008, doi: 10.1039/B713764H.

[52] P. Saffari, A. Basaligheh, V. J. Sieben, and K. Moez, “An RF-Powered Wireless Temperature Sensor for Harsh Environment Monitoring With Non-Intermittent Operation,” *Ieee Trans. Circuits Syst. -Regul. Pap.*, vol. 65, no. 5, Art. no. 5, May 2018, doi: 10.1109/TCSI.2017.2758327.

[53] G. V. Kaigala *et al.*, “An inexpensive and portable microchip-based platform for integrated RT–PCR and capillary electrophoresis,” *Analyst*, vol. 133, no. 3, Art. no. 3, Feb. 2008, doi: 10.1039/B714308G.

[54] M. Mowlem *et al.*, “Industry Partnership: Lab on Chip Chemical Sensor Technology for Ocean Observing,” *Front. Mar. Sci.*, vol. 8, 2021, Accessed: Feb. 20, 2022. [Online]. Available: https://www.frontiersin.org/article/10.3389/fmars.2021.697611

APPENDIX A TABLES OF SIMULATION PARAMETERS

Table 5 Standard chip dimensions in COMSOL simulations.

Part	Material	State	width	depth	height	x	y	z
Plate 1	PMMA	Solid	0.05	0.04	0.006	0	0	0.003
Plate 2	PMMA	Solid	0.05	0.04	0.006	0	0	0.009
Plate 3	PMMA	Solid	0.05	0.04	0.006	0	0	-0.003
Plate 4	PMMA	Solid	0.05	0.04	0.006	0	0	-0.009
Water channel	Water	Fluid	0.025	0.0004	0.0004	0	0	0.0002
Metal platform	Steel	Solid	0.27	0.26	0.04	0	0	-0.032

Part	Material	State	Radius	Height	x	y	z
Heating wire	Nichrome	Solid	0.00015	0.065	-0.0325	0.001	0.00015

Table 6 Insulated chip dimensions in COMSOL simulations.

Part	Material	State	width	depth	height	x	y	z
Plate 1	PMMA	Solid	0.05	0.04	0.006	0	0	0.003
Plate 2	PMMA	Solid	0.05	0.04	0.006	0	0	0.009
Plate 3	PMMA	Solid	0.05	0.04	0.006	0	0	-0.003
Plate 4	PMMA	Solid	0.05	0.04	0.006	0	0	-0.009
Air pocket	Air	Fluid	0.04	0.01	0.0012	0	0	0
Bridge top	PMMA	Solid	0.04	0.0034	0.003	0	0	0.0015
Bridge bottom	PMMA	Solid	0.04	0.0034	0.003	0	0	-0.0015
Water channel	Water	Fluid	0.025	0.0004	0.0004	0	0	0.0002
Metal platform	Steel	Solid	0.27	0.26	0.04	0	0	-0.032

Part	Material	State	Radius	Height	x	y	z
Heating wire	Nichrome	Solid	0.00015	0.065	-0.0325	0.001	0.00015

Table 7 Standard chip with thermocouple dimensions in COMSOL simulations.

Part	Material	State	width	depth	height	x	y	z
Plate 1	PMMA	Solid	0.05	0.04	0.006	0	0	0.003
Plate 2	PMMA	Solid	0.05	0.04	0.006	0	0	0.009
Plate 3	PMMA	Solid	0.05	0.04	0.006	0	0	-0.003
Plate 4	PMMA	Solid	0.05	0.04	0.006	0	0	-0.009
Water channel	Water	Fluid	0.025	0.0004	0.0004	0	0	0.0002
Metal platform	Steel	Solid	0.27	0.26	0.04	0	0	-0.032

Part	Material	State	Radius	Height	x	y	z
Heating wire	Nichrome	Solid	0.00015	0.065	-0.0325	0.001	0.00015
Fiberglass sheath	Fiberglass	Solid	0.001	0.04	0	0	0
Alumel wire	Alumel	Solid	0.0002	0.04	0.00025	0	0
Chromel wire	Chromel	Solid	0.0002	0.04	-0.00025	0	0

Table 8 Insulated chip with thermocouple dimensions in COMSOL simulations.

Part	Material	State	width	depth	height	x	y	z
Plate 1	PMMA	Solid	0.05	0.04	0.006	0	0	0.003
Plate 2	PMMA	Solid	0.05	0.04	0.006	0	0	0.009
Plate 3	PMMA	Solid	0.05	0.04	0.006	0	0	-0.003
Plate 4	PMMA	Solid	0.05	0.04	0.006	0	0	-0.009
Air pocket	Air	Fluid	0.04	0.01	0.0012	0	0	0
Bridge top	PMMA	Solid	0.04	0.0034	0.003	0	0	0.0015
Bridge bottom	PMMA	Solid	0.04	0.0034	0.003	0	0	-0.0015
Water channel	Water	Fluid	0.025	0.0004	0.0004	0	0	0.0002
Metal platform	Steel	Solid	0.27	0.26	0.04	0	0	-0.032

Part	Material	State	Radius	Height	x	y	z
Heating wire	Nichrome	Solid	0.00015	0.065	-0.0325	0.001	0.00015
Fiberglass sheath	Fiberglass	Solid	0.001	0.04	0	0	0
Alumel wire	Alumel	Solid	0.0002	0.04	0.00025	0	0
Chromel wire	Chromel	Solid	0.0002	0.04	-0.00025	0	0

Table 9 Material properties for COMSOL simulations.

	Thermal conductivity W/(m·K)	Heat capacity at constant pressure J/(kg·K)	Density kg/m³	Electrical conductivity(S/m)	Relative permittivity
Nichrome	5.927166+0.01766765*T^1	376.220636+0.253126352*T^1-2.04382501E-5*T^2	8617.679-0.2646861*T^1-1.012735E-4*T^2	948000	1

	Thermal conductivity W/(m·K)	Heat capacity at constant pressure J/(kg·K)	Density kg/m³	Ratio of specific heats
PMMA	0.1510983+1.344534E-4*T^1	1466	1082.529+0.974361*T^1-0.002073609*T^2	
Water	-0.869083936+0.00894880345*T^1-1.58366345E-5*T^2+7.97543259E-9*T^3	12010.1471-80.4072879*T^1+0.309866854*T^2-5.38186884E-4*T^3+3.62536437E-7*T^4	273.15 to 293.15 0.000063092789034*T^3-0.060367639882855*T^2+18.9229382407066*T-950.704055329848 293.15 to 373.15 0.000010335053319*T^3-0.013395065634452*T^2+4.969288832655160*T+432.257114008512	1+(T/Cp(T))*(alpha_p(T)*cs(T))^2

	Thermal conductivity W/(m·K)	Heat capacity at constant pressure J/(kg·K)	Density kg/m³	Ratio of specific heats
steel	43	390.15549+0.360644608*T^1-4.47692602E-4*T^2+6.0790633E-7*T^3	7911.3-0.01678428*T^1-8.018711E-4*T^2+1.172796E-6*T^3-1.015971E-9*T^4+3.677737E-13*T^5	
Alumel	100 to 400 9.346236+0.1204046*T^1-2.33021E-4*T^2+1.774554E-7*T^3 400 to 773 39.91124-0.08021887*T^1+1.89707E-4*T^2-1.037644E-7*T^3	100 to 410 - 120.397194+4.83234846*T^1 - 0.0141451249*T^2+1.51245324E-5*T^3 410 to 450 4215.99923-16.6533325*T^1+0.018666665*T^2	8610	
Chromel	13.1709-0.02474581*T^1+2.79175E-4*T^2-6.862022E-7*T^3+6.09438E-10*T^4	-169.134351+5.88577506*T^1 - 0.0235877058*T^2+4.4783402 2E-5*T^3-3.21153924E-8*T^4	8670.0	
Air	-0.00227583562+1.15480022E-4*T^1-7.90252856E-8*T^2+4.11702505E-11*T^3-7.43864331E-15*T^4	1047.63657-0.372589265*T^1+9.45304214E-4*T^2-6.02409443E-7*T^3+1.2858961E-10*T^4	d(pA*0.02897/R_const/T,pA) d(pA*0.02897/R_const/T,T)	1.4

	Thermal conductivity W/(m·K)	Heat capacity at constant pressure J/(kg·K)	Density kg/m³	Ratio of specific heats
Fiberglass	-8.216562+0.06949307*T^1-1.927595E-4*T^2+1.766669E-7*T^3	-465.069173+3.85523383*T^1-0.0103656424*T^2+9.1715623E-6*T^3	69.29	